Czech Technical University in Prague
Faculty of Nuclear Sciences and Physical Engineering

Department of Physical Electronics
Field of study: Physical Electronics
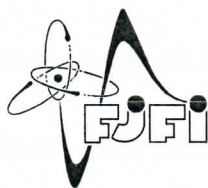**Specialization: Laser Physics and Technology**

Využití nanočástic při urychlování elektronů laserem

Nanoparticle-Assisted Laser Wakefield Electron Acceleration

MASTER'S THESIS

Author: Bc. Alžběta Špádová
Supervisor: Ing. Michal Nevrkla, Ph.D.
Consultant: Ing. Sebastian Lorenz
Year: 2023

ČESKÉ VYSOKÉ UČENÍ TECHNICKÉ V PRAZE

FAKULTA JADERNÁ A FYZIKÁLNĚ INŽENÝRSKÁ

Katedra fyzikální elektroniky

ZADÁNÍ DIPLOMOVÉ PRÁCE

Student:	**Bc. Alžběta Š p á d o v á**
Studijní program:	**Fyzikální elektronika**
Specializace:	**Laserová fyzika a technika**
Akademický rok:	**2022/2023**
Název práce: (česky)	**Využití nanočástic při urychlování elektronů laserem**
Název práce: (anglicky)	**Nanoparticle-Assisted Laser Wakefield Electron Acceleration**
Jazyk práce:	**Angličtina**

Cíl práce:

V práci se studentka bude věnovat tématu návrhu nanočásticového terče pro urychlování elektronů laserem (Nanoparticle-Assisted Laser Wakefield Electron Acceleration, NA-LWFA). Cílem práce je vylepšení simulačních nástrojů a metod pro modelování plazmových procesů v nanočásticovém terči, který je ozářený vysoce intenzivním laserovým pulzem. Pomocí navržených metod budou provedeny parametrické studie vlastností a polohy nanočástic v konkrétních terčích.

Pokyny pro vypracování

1. V návaznosti na bakalářskou práci a výzkumný úkol rozšiřte své znalosti v oblasti LWFA a podrobněji prostudujte možnosti Particle-in-Cell (PIC) simulací.
2. Proveďte rešerši vhodných přístupů pro realizaci 3D PIC simulace, případně zvažte využití cylindrické geometrie. Vyberte nejvhodnější metodu pro modelování nanočásticového terče.
3. Pomocí navržených metod studujte vliv parametrů nanočástic na injekci elektronů do urychlující fáze a na energetické spektrum urychlených elektronů v konkrétních terčích používaných pro LWFA experimenty v ELI-Beamlines.

Doporučená literatura:

1. Cho M. H. et. al., Controlled electron injection facilitated by nanoparticles for laser wakefield acceleration, Scientific Reports, 2008, vol. 8, p. 1-8.
2. Aniculaesei C. et. al., Proof-of-principle experiment for nanoparticle-assisted laser wakefield electron acceleration, Physical Review Applied, 2019, vol. 12, no. 4, p. 41-51.
3. Birdsall C. K., Langdon A. B., Plasma Physics via Computer Simulation (Series on Plasma Physics), Taylor & Francis, 1991, ISBN 0750301171.
4. Esarey E. et. al., Physics of laser-driven plasma-based electron accelerators, Reviews of Modern Physics, 2009, vol. 81, p. 1229.

Jméno a pracoviště vedoucího práce:

Ing. Michal Nevrkla, Ph.D.
Katedra fyzikální elektroniky, Fakulta jaderná a fyzikálně inženýrská ČVUT v Praze
FzÚ AV ČR, v.v.i., projekt ELI-Beamlines

Jméno a pracoviště konzultanta:

Ing. Sebastian Lorenz
Katedra fyzikální elektroniky, Fakulta jaderná a fyzikálně inženýrská ČVUT v Praze
FzÚ AV ČR, v.v.i., projekt ELI-Beamlines

Datum zadání: 4. říjen 2022

Datum odevzdání: 3. květen 2023

Doba platnosti zadání je dva roky od data zadání.

....
Garant oboru

....
Vedoucí katedry

....
Děkan

V Praze dne 4. 10. 2022

Prohlášení

Prohlašuji, že jsem diplomovou práci vypracovala samostatně a použila jsem pouze podklady (literaturu, projekty, SW atd.) uvedené v přiloženém seznamu.

V Praze dne 2.5.2023

Bc. Alžběta Špádová

Acknowledgements

<div align="right">Bc. Alžběta Špádová</div>

Název práce:

Využití nanočástic při urychlování elektronů laserem

Vypracovala:	Bc. Alžběta Špádová

Studijní program:	Fyzikální elektronika
Specializace:	Laserová fyzika a technika
Druh práce:	Diplomová práce

Vedoucí:	Ing. Michal Nevrkla, Ph.D.
	Katedra fyzikální elektroniky, Fakulta jaderná a fyzikálně inženýrská ČVUT v Praze
	FzÚ AV ČR, v.v.i., projekt ELI-Beamlines
Konzultant:	Ing. Sebastian Lorenz
	Katedra fyzikální elektroniky, Fakulta jaderná a fyzikálně inženýrská ČVUT v Praze
	FzÚ AV ČR, v.v.i., projekt ELI-Beamlines

Abstrakt: Práce se zabývá principem urychlování elektronů pomocí ultrakrátkých, vysoce intenzivních, laserových impulsů. Je v ní popsáno nově navržené schéma využívající plynový terč obsahující nanočástice a jsou zmíněny jeho hlavní výhody v porovnání s ostatními injekčními schématy. Dále je rozebrána metoda particle-in-cell, hojně využívaná pro studium interakce laserového záření s plazmatem, a v krátkosti jsou představeny dva různé particle-in-cell kódy (Smilei a WarpX). Cílem práce je pomocí numerických simulací navrhnout nanočásticový plynový terč, který by byl vhodný pro použití při experimentech na ELI Beamlines. Kvůli vysokým nárokům na rozlišení, které plynou z přítomnosti nanočástic, jsou simulace provedeny v kvazi-cylindrické geometrii. Výsledky simulací jsou následně důkladně analyzovány a na jejich základě je proveden konečný návrh nanočásticového plynového terče.

Klíčová slova: LWFA, nanočástice, elektronová injekce, PIC simulace

Title:

Nanoparticle-Assisted Laser Wakefield Electron Acceleration

Autor:	Bc. Alžběta Špádová

Abstract: This master's thesis deals with principles of electron acceleration driven by high-intensity, ultrashort laser pulses. Newly designed electron injection scheme utilising gas target containing nanoparticles and its major benefits are described. Furthermore, a description of particle-in-cell method, widely used for the study of laser-plasma interaction, is provided together with a short introduction of two different particle-in-cell codes (Smilei and WarpX). This thesis aims at designing designing a nanoparticle gas target suitable for experiments realized at ELI Beamlines via PIC simulations. Due to high computational requirements emerging from the presence of nanoparticles, simulations are ran in quasi-cylindrical geometry. The results are then thoroughly analysed and based on them the nanoparticle gas target is designed.

Key words: LWFA, nanoparticle, electron injection, PIC simulations

Contents

Introduction

A number of fundamental questions on the nature of matter and energy have been resolved thanks to the use of particle accelerators. Mechanism of conventional accelerators is based on radio-frequency technology, limiting the maximum achievable accelerating gradient. Accelerators, based on plasma wakefield generated by high-intensity laser, are capable of sustaining much higher accelerating gradients [1]. Therefore, this approach is more convenient in terms of cost and compactness.

Accelerated electrons have a wide range of practical applications with high social and economic impact. They can be used as sources of coherent high-brightness radiation with wavelengths ranging from x-rays to gamma-rays. These sources have great potential for applications in fields such as biology and medicine (e.g., single-particle imaging, cancer treatment via radiotherapy, tumor imaging, or sterilization of medical devices). Another possible utilization is non-destructive testing using radiography for safety and defense purposes or pulse radiolysis [2].

Although laser wakefield acceleration has already demonstrated multi-GeV energies [3], small energy spreads [4], and high-charge electron beams [5], the process of controllable electron injection, enabling utilization in the above-mentioned fields, is still a great challenge [6]. The easiest way to inject the electrons into the accelerating phase of a plasma wave is the self-injection; in this case, the amplitude of the wakefield exceeds the critical value and the plasma wave breaks. Since it is impossible to precisely predict when this phenomenon occurs, we are not able to control the process of electron injection.

A recently proposed injection scheme, using gas targets with diffused nanoparticles, could be the solution to this issue. In [7] and [8] authors carried out Particle - in - Cell (PIC) simulations suggesting a significant advancement towards the electron beam energy, energy spread and divergence compared with the case of self-injection. Moreover, these simulations demonstrated the possibility of controlling the total charge of the injected electron beam by the position, number, size, and density of the nanoparticles [7]. Furthermore, this injection scheme enables decoupling of the electron injection from laser evolution, which is very desirable for generating a stable multi-GeV electron bunches [9], since reaching energies this high is not possible without laser guiding. Most of these exceptional benefits of the injection scheme using nanoparticles were also confirmed by experiments [8] and [9].

This work focuses on designing a gas target taking advantage of this new injection scheme and suitable for future experiments at ELI Beamlines. More precisely, two experiments have been taken into consideration, one with kHz laser L1 Allegra, called ALFA, and a second one with petawatt laser L3 HAPLS, which is called ELBA. In the first experiment, the gas target is quite short - less than 1 mm, hence the nanoparticles can be used as a way to achieve controllable injection. However, setting up the experiment could be very challenging, since nanoparticles need to be

delivered into the gas target at a relatively precise location. Nevertheless, for the ELBA experiment, which currently uses gas target about 20 mm long, this injection scheme seems to be very suitable. Laser parameters and the gas target length used in ELBA experiment allows to fully exploit all the advantages of the nanoparticle injection scheme, whereas the required precision in the experiment setup is not as critical as in the ALFA experiment.

The first chapter of this thesis provides a brief overview of the LWFA technique including the basic principles of laser plasma interaction, limitations of the LWFA method, as well as a description of several injection schemes, with emphasis on the one using nanoparticles. In the second chapter, a widely used numerical method for plasma physics, Particle-in-Cell, is discussed in detail. Chapter three contains a description of advanced numerical methods used in PIC simulations. Their purpose is to reduce the simulation run time and make them less computationally expensive, while making more or less strict assumptions. Fourth chapter is dedicated to a comparison of the computational cost and results from full 3D and quasi-3D PIC simulations. Finally, the fifth chapter is focused on evaluation of results obtained from numerous PIC simulations studying the influence of the nanoparticle parameters, such as material or size, on the electron injection process and parameters of the accelerated electron beam.

Chapter 1

Laser wakefield acceleration

Laser plasma accelerators have drawn the wide attention of the scientific community as a promising way of constructing compact high-energy electron accelerators. This mechanism uses plasma waves generated via the interaction of intense ultrashort laser pulses with gas targets to capture and accelerate electrons to relativistic velocities. Although these accelerators have a high potential to replace conventional accelerators in the future, the quality of generated beams has to be further improved.

Since electron injection is one of the key features determining the beam characteristics, several injection mechanisms yielding better electron beam parameters were proposed over the last twenty years. The most recent and very promising scheme utilizes a gas target containing nanoparticles. These targets could allow us to precisely control the location where the electrons are being injected into the wakefield, as well as to improve some other important beam parameters.

1.1 Laser propagation in a vacuum

In optics, and particularly in laser physics, laser beams often occur in the form of Gaussian beams and LWFA experiments are not an exception. Although, strictly speaking, the beams are not exactly Gaussian, it is still a very good approximation. This is why, at the beginning of this chapter, the properties and propagation of Gaussian beams will be described.

The electric field of a laser beam, propagating along the z-axis, can be described using the following expression [10]:

$$E(r, z) = E_0 \frac{w_0}{w(z)} f(r, z) g(t, z) \cos(\omega_L t - k_L \left(z + \frac{r^2}{2R(z)} \right) + \varphi_L) \vec{e}_{pol} + \text{cc.,} \quad (1.1)$$

where

$$f(r, z) = \exp\left(-\frac{r^2}{w(z)^2} \right) \quad \text{and} \quad g(t, z) = \exp\left(-\frac{(t - \frac{z}{c})^2}{\tau_0^2} \right). \quad (1.2)$$

The function $f(r, z)$ describes the radial envelope with the transverse radius of the beam $w(z)$ and $g(t, z)$ represents temporal envelope with τ_0 as the pulse duration defined at $1/e$ of the electric field. The meaning of remaining terms is as follows: ω_L is the laser carrier angular frequency, k_L is the wavenumber, w_0 is the beam waist, that is the radius at $1/e$ of the electric field in the focal plane (z=0). Finally, e_{pol} is the vector describing the polarization of the laser pulse and E_0 is the amplitude of the electric field.

1.1.1   Gaussian beam parameters

The propagation of the Gaussian laser pulse is fully characterized by the beam waist $w(z)$, the radius of curvature of the wavefront $R(z)$, and the Gouy phase shift $\varphi(z)$. These parameters vary as the laser beam propagates, which can be described mathematically as [11]:

$$w(z) = w_0 \sqrt{1 + \left(\frac{z}{z_R}\right)}, \tag{1.3a}$$

$$R(z) = z\left(1 + \left(\frac{z_R}{z}\right)^2\right), \tag{1.3b}$$

$$\varphi_L(z) = \arctan\left(\frac{z}{z_R}\right). \tag{1.3c}$$

Here z_R stands for Rayleigh length of a laser beam, representing the position at which the laser beam transverse area is doubled, compared with the one in the focal plane:

$$z_R = \frac{\pi w_0^2}{\lambda_L}, \tag{1.4}$$

where λ_L is the laser wavelength. Another important parameter of the Gaussian beam is the beam divergence, which is defined far away from the focal plane as:

$$\tan\theta \approx \theta \approx \frac{\Delta w(z)}{\Delta z} = 2\frac{\lambda_L}{\pi w_0}. \tag{1.5}$$
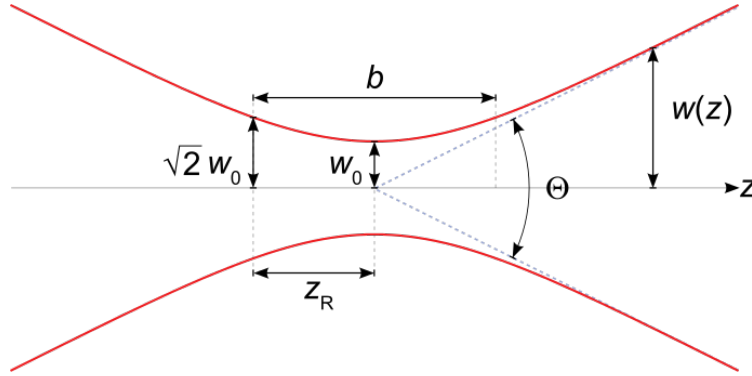
Figure 1.1: Representation of the envelope of a Gaussian laser beam with depicted parameters [12].

1.1.2   Gaussian beam intensity

The intensity of laser beam can be defined as a cycle-averaged Poynting vector:

$$I_L = \langle \vec{S} \rangle_T = c^2 \varepsilon_0 \langle \vec{E} \times \vec{B} \rangle_T = \frac{c\varepsilon_0}{2}|\vec{E}|^2, \tag{1.6}$$

where ε_0 is the vacuum permittivity and T is one optical cycle. Since the intensity of a Gaussian beam in the plane transverse to the propagation has a gaussian-shape profile as well, we can write:

$$I(r,z) = I_0 \exp\left(-2\frac{r^2}{w^2(z)}\right), \qquad I_0 = \frac{2P}{\pi w^2(z)} \tag{1.7}$$

where P is the power of the beam.

It is convenient to know the relations between the characteristics used for Gaussian beam description (beam waist w_0 and the pulse duration τ_0) and measurable quantities at FWHM (Full Width Half Maximum) of the temporal and spatial intensity profile (the spot size d_{FWHM} and pulse duration t_{FWHM}). These relations stand as follows:

$$t_{FWHM} = \sqrt{2ln(2)}\tau_0, \qquad d_{FWHM} = \sqrt{2ln(2)}w_0. \tag{1.8}$$

1.2 Basics of plasma physics

Plasma is often referred to as the fourth state of matter and it is the most common form of matter in the universe. However, it does not occur naturally on the Earth's surface, apart from a few exceptions like flashes of lighting bolts. For studying plasma, it can be created artificially in laboratories, usually by ionization of gas (for example using a laser).

Plasma consists of lighter electrons and much heavier positive ions, hence, it is electrically conductive. This is what primarily distinguishes plasma from solids, liquids, and gases. Despite the presence of electrically charged particles, plasma appears neutral from the macroscopic view, this phenomenon is called quasi-neutrality [13]. This fact can be mathematically expressed as:

$$\sum_s q_s n_s \approx 0, \tag{1.9}$$

where q_s is the charge and n_s is density of particles of species s. Nevertheless, at smaller scales, a charge imbalance can occur, which may cause the presence of local electric fields. Another characteristic of plasma is so-called collective behavior. Meaning, that even though the particles are not bound, they respond to electromagnetic fields as a whole - rather like a fluid than a group of free particles.

A slightly different approach to describing quasi-neutrality leads to a very important quantity characterizing plasma called the Debye Length λ_D. The Debye length is the distance over which a charge q is shielded by particles with opposite charge. In other words, an ion (or electron) gathers a shielding cloud of electrons (or ions) that tend to cancel its own charge [14] and the Debye length is an approximate radius of this cloud. For electrons λ_{De} can be expressed as [14], [15]:

$$\lambda_{De} = \sqrt{\frac{T_e}{4\pi n_e e^2}} = \sqrt{\frac{\varepsilon_0 k_B T_e}{e^2 n_e}}, \tag{1.10}$$

where T_e is the electron temperature. An expression for ions is analogous.

An ideal plasma has many particles in a Debye sphere, which is a premise for Debye shielding (and collective behaviour) discussed earlier. Therefore, we establish another important plasma parameter, which is dimensionless and indicates a number of particles per Debye sphere:

$$N_D = \frac{4\pi}{3} n_s \lambda_{De}^3. \tag{1.11}$$

Hence, in an ideal plasma $N_D \gg 1$ must hold.

1.2.1 Laser propagation in a plasma

In contrast to vacuum, not every laser beam is able to propagate in a plasma medium. Because of the dispersion relation of a laser pulse interacting with a plasma:

$$\omega_L^2 = \omega_p^2 + c^2 k^2. \tag{1.12}$$

Here ω_p is the plasma frequency defined as:

$$\omega_p = \sqrt{\omega_{pe}^2 + \omega_{pi}^2}, \tag{1.13}$$

where ω_{pe} and ω_{pi} are electron plasma frequency and ion plasma frequency, respectively. Since the ions are much heavier than electrons, their plasma frequency is much lower. Moreover, they do not respond to the high-frequency oscillations of the laser electric field. Thus, in many of the phenomena, including LWFA, the ions can be treated as immobile [16].

Because the electron plasma frequency is one of the most fundamental characteristics in plasma physics, it is necessary to include its definition:

$$\omega_{pe} = \sqrt{\frac{n_e e^2}{\varepsilon_0 m_e}}, \tag{1.14}$$

where n_e is the electron density. In LWFA experiments, the electron density n_e is of the order of $10^{17} - 10^{20}$ cm^{-3} [17]. Note that ion plasma frequency would be defined analogously.

From equation (1.12) follows that if the laser frequency ω_L is lower than the plasma frequency ω_p, the laser beam cannot propagate through it [12]. This allows us to introduce the concept of a critical density for the laser pulse, corresponding to the maximum density at which the laser can propagate. Similarly, it is possible to distinguish *underdense* plasma ($\omega_L > \omega_p$), which allows laser pulse propagation, and *overdense* plasma ($\omega_L < \omega_p$), which does not.

Depending on the laser wavelength it is possible to define critical density n_c as:

$$n_c = \frac{m_e \varepsilon_0 \omega_L^2}{e^2} \simeq \frac{1.1 \times 10^{21}}{\lambda_L^2 [\mu m]}. \tag{1.15}$$

1.2.2 Normalized vector potential

An important parameter in the discussion of intense laser-plasma interactions is the laser's normalized peak vector potential a_0 (also called the laser strength parameter) [17]:

$$a_0 = \frac{e E_0}{m_e \omega_L c} = \frac{e A_0}{m_e c}, \tag{1.16}$$

where e is the elementary charge, m_e is the electron mass and A_0 is the maximum value of laser's vector potential $\vec{A}$. This quantity distinguishes the nonrelativistic ($a_0 \ll 1$) and the relativistic regime ($a \geq 1$).

Using equation (1.6) as a relation between I_0 and E_0 and expression $\omega_L = \frac{2\pi c}{\lambda_L}$ we obtain useful relation:

$$a_0 = \sqrt{\frac{e^2}{2\pi \varepsilon_0 m_e^2 c^5} \lambda_L^2 I_0} \simeq 0.85 \sqrt{I_0 [10^{18} W/cm^2]} \cdot \lambda_L [\mu m]. \tag{1.17}$$

For example, for a laser system operating at wavelength $\lambda_L = 850$ nm $a_0 = 1$ corresponds to laser intensity $I_0 \approx 2.16 \times 10^{18}$ W/cm^2.

1.3 Excitation of plasma waves

The mechanism of laser wakefield accelerators is based on ultra-intense ultra-short laser pulses passing through a neutral gas, which is thereby ionized, creating plasma. For the generation of plasma, the rising edge of the laser pulse is usually sufficient. Therefore, the main part of the pulse interacts directly with underdense plasma, displacing electrons from their equilibrium positions. Thus, exciting a longitudinal plasma wave moving behind the laser pulse.

This plasma wave creates an electric field called *wakefield* with an intensity of about 100 GV/m, which is about three orders more than in conventional accelerators. The phase velocity of the plasma wave $v_{\varphi p}$ is the same as the group velocity of driving laser pulse v_{gL} and its wavelength depends on the electron density as:

$$\lambda_p = 2\pi c \sqrt{\frac{m_e \varepsilon_0}{n_e e^2}} = \frac{2\pi c}{\omega_p}, \tag{1.18}$$

whereas this relation is valid in the nonrelativistic regime ($a_0 \ll 1$). For example, for electron density $n_e = 10^{18}$ cm^{-3}, the resulting plasma wave wavelength is $\lambda_p = 33$ μm. Here, as well, is possible to use an approximate expression [10]:

$$\lambda_p[\mu m] \simeq \frac{33.4}{\sqrt{n_e[10^{18} cm^{-3}]}}. \tag{1.19}$$
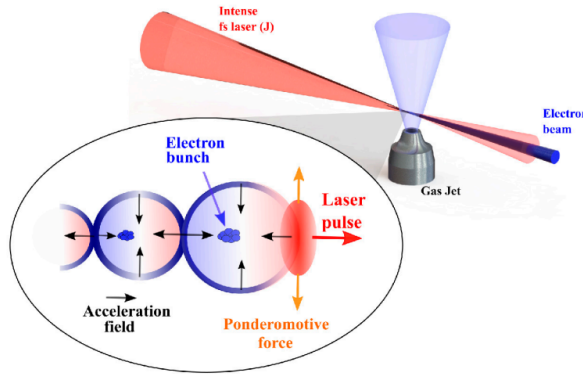
Figure 1.2: LWFA mechanism scheme [18].

1.3.1 The ponderomotive force

The force responsible for the rise of the plasma wave is called ponderomotive force. It is a nonlinear force representing the gradient of the laser intensity that pushes charged particles into the region of a weaker field. Note that electrons and ions are pushed in the same direction. In the non-relativistic case, the ponderomotive force can be expressed by the following relation [10]:

$$\vec{F}_p = -\frac{e^2}{4m\omega_L^2} \nabla(E_0^2) = -\frac{m_e c^2}{2} \nabla(a_0^2), \tag{1.20}$$

where E_0 is the electric field amplitude. From this relation follows that the electrons are strongly influenced by this force, because of their low mass. On the other hand the force acting on much heavier ions is in most cases negligible.

For particles moving with velocities close to the speed of light c, it is necessary to account for the relativistic effects. This occurs in nonlinear regime ($a_0 \geq 1$) and the expression in this case is [19]:

$$\vec{F}_p = -\frac{m_e c^2}{2\sqrt{1 + a_0^2}} \nabla(a_0^2).$$

(1.21)

1.3.2   Linear plasma waves

To describe the plasma waves emerging as a consequence of ponderomotive force displacing electrons from their equilibrium positions and causing a density perturbation, one can use following two equations [20]:

$$n_s m_s \frac{d\vec{u}_s}{dt} = n_s q_s (\vec{E} + \vec{u}_s \times \vec{B}) - \nabla P_s,$$

(1.22)

$$\frac{\partial n_s}{\partial t} + \nabla(n_s \vec{u}_s) = 0.$$

(1.23)

These expressions are called Lorentz and continuity equation, respectively. Since they are used to describe plasma under assumptions that each charged particle component of density n_s and velocity $\vec{v}_s$ behaves in a fluid-like manner, interacting with other species (s) via the electric and magnetic fields [20], these expressions are commonly called fluid equations.

Equations (1.22) and (1.23) can be further simplified assuming stationary ions ($\vec{v}_i = \vec{0}$), the cold fluid limit ($\nabla P_s = 0$) and small perturbations compared to equilibrium state ($\delta n \ll n_0$). In the linear regime (low intensity laser ($a_0 \ll 1$)) we obtain following equations for the density perturbation δn_e [17]:

$$\left(\frac{\partial^2}{\partial t^2} + \omega^2\right) \frac{\delta n_e}{n_0} = c^2 \nabla^2 \left(\frac{a^2}{2}\right),$$

(1.24)

and the electric field of the wave $\vec{E}$ [17]:

$$\left(\frac{\partial^2}{\partial t^2} + \omega^2\right) \phi = \omega^2 \left(\frac{a^2}{2}\right),$$

(1.25)

where $\delta n / n_0$ is the normalized density perturbation associated with the electrostatic wake ϕ [17], which can be described via the Poisson's equation [10]:

$$\nabla^2 \phi = e \frac{\delta n_e}{\varepsilon_0}.$$

(1.26)

The solution to (1.24) and (1.25) can be found in the following form:

$$\frac{\delta n_e}{n_0} = \frac{c^2}{\omega_p} \int_0^t \sin[\omega_p(t - t')] \nabla^2 \frac{|\vec{a}(\vec{r}, t')|^2}{2} dt'$$

(1.27)

and:

$$\frac{\vec{E}}{E_0} = -c \int_0^t \sin[\omega_p(t - t')] \nabla^2 \frac{|\vec{a}(\vec{r}, t')|^2}{2} dt'.$$

(1.28)

Here, ω_p is the frequency of created plasma wave. Hence, in case of the linear regime, the plasma wave has a sinusoidal shape. Note that these equations are valid only

for small density perturbations ($\delta n_e \ll n_0$) and electric field much smaller than the cold non-relativistic wave breaking limit ($E \ll E_0$) [17]:

$$E_0 = \frac{m_e c \omega_p}{e} \simeq 96\sqrt{n_e[10^{18}\mathrm{cm}^{-3}]}\mathrm{GVm}^{-1}. \tag{1.29}$$

Here E_0 is also called the cold non-relativistic wave breaking field [21].

1.3.3 Nonlinear plasma waves and wave breaking

The approximation of small density perturbations is inadequate for describing plasma waves driven by strong laser pulses ($a_0 \gg 1$) used for LWFA. In this case the electric field of plasma wave is strong and nonlinear, plasma wavefronts become farther apart and the plasma waves more peaked. (see fig. 5 1.3).
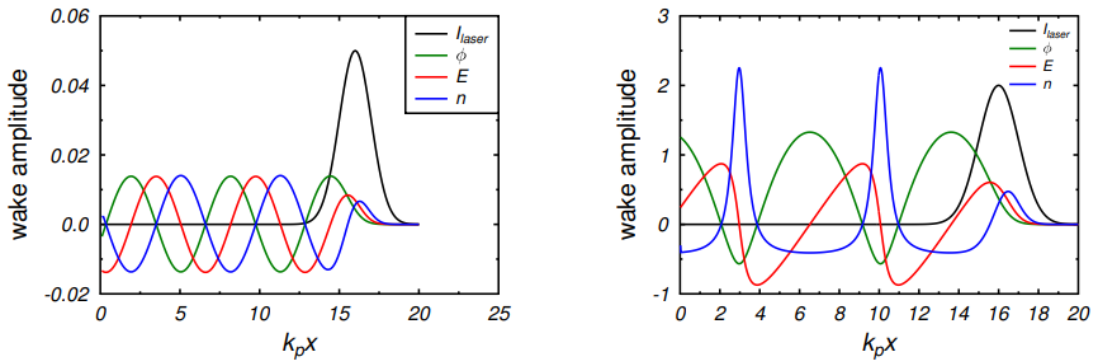
Figure 1.3: Comparison between linear and nonlinear plasma waves. Note the sinusoidal profile in the linear case (left) and a *sawtooth* profile in the nonlinear regime (right) [20].

In the nonlinear regime, the wave propagation velocity depends on the wave amplitude, which can exceed the value E_0. To reach relativistic wave breaking in a cold plasma, it is necessary to obtain electric fields with an amplitude of approximately [22]:

$$E_{WB} = \sqrt{2(\gamma_p - 1)}E_0, \qquad \gamma_p = \left(1 - \frac{v_\varphi^2}{c^2}\right)^{-\frac{1}{2}} \tag{1.30}$$

where γ_p is the relativistic Lorentz factor associated with the phase velocity of the plasma wave. Let us remind that the plasma wave phase velocity is approximately the group velocity of the laser.

As the amplitude of the plasma wave approaches the value of wave breaking limit E_{WB}, the velocity of the background electrons can exceed the phase velocity of the plasma wave. This leads to a breakdown of the wakefield structure. During this process, some electrons, initially a part of the plasma wave, leave the wave and can be trapped by an accelerating field. Note that this loss of electrons causes the decrease of the plasma wave amplitude [23].

This mechanism is called self-injection, and from an experimentalist's point of view, it is the most straightforward way to inject electrons into the accelerating phase of the plasma wave. In comparison with other proposed schemes, which will be discussed later, it does not require synchronization while performing the experiment. Also, it is not necessary tend that electrons are injected in the proper phase of the wave, i.e. in the phase space region where the wave is both focusing and accelerating [24].

Naturally, there are several disadvantages to using this mechanism, such as the inability to control the number of injected electrons or the place and time when the injection occurs. Consequently, obtained electron bunches have quite a wide energy spread and the achievable beam energy is limited.

1.4 Electron injection schemes

Because parameters of accelerated electron beams are crucial for potential applications, it is desirable to find means that would improve their quality (i.e. high energy and charge, small energy spread, and low divergence). Since electron injection is one of the key features determining the beam characteristics, several injection mechanisms yielding better electron beam parameters were proposed over the last twenty years.

For standard LWFA experiments internal electron injection is usually used. The reason is that using electron bunches created in another accelerator (external injection), presents huge experimental issues due to synchronization, the satisfaction of the condition of electron bunch length being small compared to practical plasma wavelength, and the fact that electrons must be injected in the proper phase of the wave [25]. However, lately, a recent article in Nature [26] have suggested the use of a dual-stage acceleration (i.e. using two separated plasma mediums, hence, using two different wakefields for accelerating electron) for obtaining beams with multi-GeV energies, successfully confronting these challenges.

Nevertheless, this thesis deals with the injection scheme using nanoparticles, which belong to internal injection mechanisms. Hence, in the following section, some of these injection schemes will be briefly discussed, whereas the main attention will be focused on the nanoparticle scheme.

1.4.1 Density transition injection

This electron injection scheme, which uses an inhomogeneous plasma with a sharp density drop ("down-ramp"), has been demonstrated to be an elegant and efficient approach for generating high-quality electron beams. In the down-ramp region, the plasma wave wavelength rises which leads to wave-breaking and the creation of stable electron bunches with low energy spread [27]. Moreover, this approach is easily implemented by inserting a sharp blade on top of the gas nozzle.

1.4.2 Ionization injection

This approach relies on the use of a gas target constituting of high-Z gas and is also quite easy to realize. The first levels of ionization occur usually after the interaction with the rising edge of the laser pulse (intensities below 10^{16} W/cm^2 are usually sufficient). Hence, these electrons are created in a region with relatively low laser intensity and thereafter form the plasma wave. On the other hand, ionization from inner shells occurs at higher intensities (typically for intensities over 10^{18} W/cm^2), so these electrons are freed close to the peak of the laser pulse; thus, they are 'born' in a trapped orbit and accelerated [28]. This method represents a straightforward way to increase the injected charge without reaching wave-breaking amplitudes, controlling the beam quality can be rather difficult.

1.4.3   Colliding pulse injection

Colliding pulse injection, also called optical injection, uses two different counter-propagating laser pulses; a main pulse (pump pulse) creates a high amplitude plasma wave and collides with a second pulse of lower intensity, which is used to trigger a localized injection, resulting in low energy spread [6]. Furthermore, this scheme offers more flexibility and enables one to separate the injection from the acceleration process. By changing the collision position, it is also possible to tune the beam energy. A downside to this injection scheme is the requirement of very precise setup and synchronization.

1.4.4   Injection scheme using nanoparticles

The most recent and very promising scheme, called Nanoparticle Assisted Laser WakeField Acceleration (NA LWFA), utilizes a gas target containing nanoparticles. These targets could allow us to precisely control the location where the electrons are being injected into the wakefield [7], [8], hence, to some extend, control the beam parameters.

The selection of suitable material, diameter, and position of the nanoparticles in the gas target enables us to design an electron accelerator producing electron beams with required parameters and high shot-to-shot stability so desirable for potential applications.
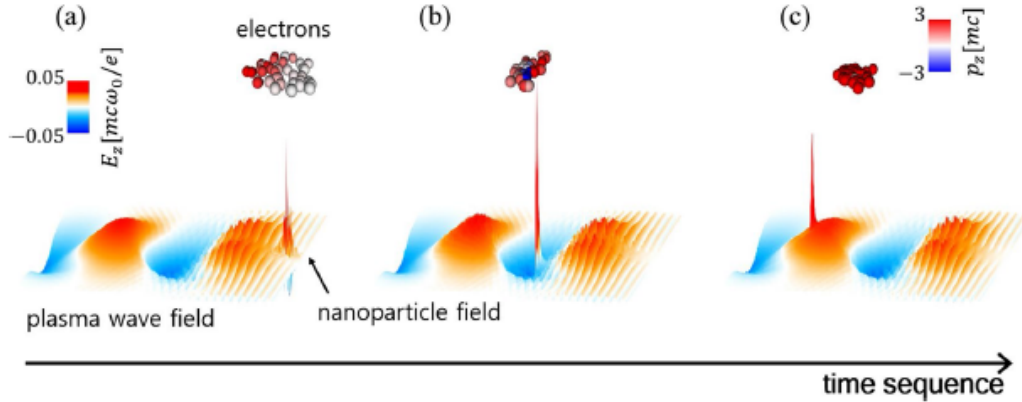
Figure 1.4: The time sequence of the electron injection process under the influence of a nanoparticle. (a) Nanoparticle field starts to grow and attracts nearby electrons. (b) The attracted electrons obtain additional momentum as a result of the interaction with the nanoparticle field and the plasma wakefield. (c) The electrons are injected into the plasma wave [7].

The principle of this method lies in setting the parameters of laser and plasma in a way that the self-injection occurs only if a nanoparticle is present in the wakefield. As the laser pulse propagates through the gas target it ionizes the gas as well as the nanoparticles. In the proximity of ionized nanoparticles, a positively charged electric field arises, being much stronger than the generated wakefield. Nearby electrons (released by the ionization of nanoparticles and also from the plasma background) are attracted to the region with a positive charge and afterward efficiently injected into the wakefield.

1.4.5   Factors influencing the beam parameters

Using the gas target with nanoparticles allows us to control the moment of electron injection, hence, the energy of the accelerated beam. The sooner the injection occurs, the longer the acceleration length and the higher the obtained energy. An experiment from [8] also proved that if the injection scheme with nanoparticles is applied, maximum achievable energies are higher than if the electrons are self-injected. There are two possible explanations, the first is already mentioned longer acceleration length. The second is that electrons are injected into the accelerating phase of the plasma wave with a lower charge, hence, the wakefield is less disrupted and the accelerating field is stronger.
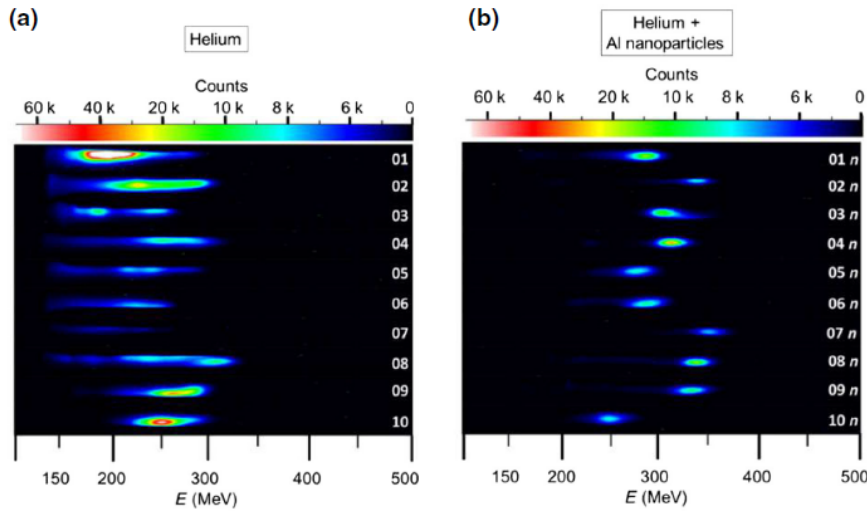
Figure 1.5: False-color images of the electron energy spectra. (a) Electron spectra generated without the presence of nanoparticles and (b) energy spectra generated with nanoparticles. Note the energy spread is significantly reduced, as compared with the case without nanoparticles. [8].

From the PIC simulations performed by Cho in 2018 [7] follows that the choice of nanoparticle material density affects the charge of the electron beam. Higher density creates a stronger nanoparticle electric field, thus, more electrons are injected, and the beam charge increases. However, it starts to saturate when the nanoparticle density reaches the saturation density, whereas the value varies according to the used laser parameters.

This phenomenon can be understood as the saturation of the nanoparticle field. It arises as a consequence of two opposing forces acting on the electrons - the repelling ponderomotive force caused by the laser pulse and the attracting force of the positively charged nanoparticles. At the moment the nanoparticle potential is balanced by the ponderomotive potential, the nanoparticle field cannot grow any further and the injected charge reaches saturation.

Another thing influencing the characteristics of the obtained electron beam is the number of ionized nanoparticles because every individual nanoparticle induces separate electron injection. A positive thing is the energy spread does not grow with the number of nanoparticles [7] since it would be nearly impossible to use only one nanoparticle in a real-life experiment.

The number of nanoparticles also affects the total beam charge. However, it is not directly proportional to the number of nanoparticles because the amount of injected

electrons, hence, the charge, depends on the transverse nanoparticle position. The reason is the wakefield weakens with the distance from its axis, and so does the injected beam charge. Nonetheless, the multiple injections can negatively influence the beam emittance (a property of a particle beam that characterizes its size). To obtain the lowest beam emittance, it is desirable to control the transverse positions of the nanoparticles within a few microns.

1.5 Limitations on energy gain

Several phenomena can limit the energy gain in the LWFA process. The main limitations are the beam loading and so-called "detrimental Ds": Diffraction, Dephasing, and Depletion. Whereas, electron dephasing and pump depletion are the hardest to overcome, which makes them the most critical limitations for reaching electron energies over 10 GeV. All these mechanisms will be briefly discussed in the following section.

1.5.1 Beam loading

Beam loading is the phenomenon which limits the charge and the beam quality in plasma based accelerators [29]. Furthermore, it causes the decrease of the electron beam energy and also the increase of the energy spread. This phenomenon occurs because the bunch of accelerated electrons drives its own plasma oscillation modifying ("beam-loading") the electric field of the plasma wave, and therefore, the acceleration process. In some cases, this phenomenon can even cancel out the laser wakefield, hence, it ultimately limits the maximum charge that can be accelerated [29].

Even before reaching this limit, beam loading can severely impact the beam quality, specifically the energy spread. This is because of the trailing electrons of the bunch are accelerated by a weaker electric field as they experience the superposition of the laser wakefield and the plasma wave driven by the leading electrons of the bunch.

This effect is, therefore, of major importance for improving the capabilities of laser-plasma accelerators. Fortunately, there are means by which beam loading can be overcome, for example, careful shaping of the electron bunch resulting in a constant total electric field over the bunch length.

1.5.2 Laser diffraction

In any focused beam, diffraction will reduce the laser intensity after a certain distance, in a vacuum, this distance is of the order of the Rayleigh length z_R (see eq. 1.3b). As the laser pulse diverges, its normalized vector potential decreases, and so does the plasma wave amplitude. Hence, without some form of optical guiding, the length of the strong accelerating field will be limited to a few z_R.

Therefore, various methods of optical guiding, such as preformed plasma density channel were proposed. However, even without this preformed channel, a high-intensity laser beam propagating in plasma can easily prevail over natural diffractive defocusing and can stay focused for a significantly longer distance than in a vacuum.

This non-linear effect, called *self-focusing*, is a consequence of the dependence of the refractive index on the laser beam intensity ($n(I) = n_0 + n_2 I$). Thus, the refractive index is higher along the axis and the plasma medium acts as a focusing lens for the laser. The power threshold P_c for this behavior to occur as approximately [30]:

$$P_c \approx 17 \times \left(\frac{\omega_L}{\omega_p} \right)^2 \text{GW}. \tag{1.31}$$

Hence, if a beam comes with power exactly at the self-focusing limit then it will exhibit self-trapping, where the laser profile remain constant over a larger distance, because diffraction divergence is completely compensated by the non-linear converging effect [30]. However, this state is very unstable and even a small deviation can disrupt the whole process.

1.5.3   Electron Dephasing

Electron dephasing is a result of highly relativistic electrons outrunning accelerating phase of the wakefield by reaching velocity higher than the plasma wave phase velocity (respectively the laser group velocity, since $v_{\varphi p} = v_{gL}$). In this manner, the electrons leave the accelerating phase of the plasma wave and "dephase" (i.e. move into decelerating phase of the wake).

The distance which an electron can travel before it crosses the zero field in the lab frame is called dephasing length L_d [10]. Which is proportional to electron density as $L_d \approx n_e^{-3/2}$, therefore, it can be diminished using lower plasma densities, albeit at longer acceleration length. For example, for $n_e \approx 5 \times 10^{18}$ cm^{-3} and $a_0 = 2$, the dephasing length is usually 3-4 mm.

The dephasing limitation could in principle be overcome by staging the laser-plasma accelerator such that, after outrunning the plasma wave, the electron is injected into a new plasma wave at the appropriate phase [31]. However, this approach would require very precise control over electron injection and laser pulses, thus, it comes with its own set of challenges.

1.5.4   Pump depletion

As the laser pulse propagates and excites the plasma wave it also loses its energy. The distance over which the pump pulse loses a significant fraction of its energy is frequently called the pump depletion length L_{pd}. In relativistic nonlinear case ($a_0 \gg 1$), this value can be estimated by equating the laser pulse energy to the energy left behind in the wake $E_L^2 L_{pd} = E_z^2 L$ (E_L is the laser field and E_z is the plasma wave field [32]) as:

$$L_{pd} \approx \frac{\lambda_p^3}{\lambda_L^2} \frac{\sqrt{2} a_0}{\pi}. \tag{1.32}$$

In this case pump depletion is comparable with electron dephasing length implying efficient use of the pump laser pulse energy.

Chapter 2

Particle-in-cell method

Laser-plasma interaction is in general complex and strongly non-linear problem to solve. Therefore, investigation of these systems using only analytical calculations and experiments is usually insufficient, and carrying out numerical simulations seems to be the only option to acquire deeper insight and investigate this phenomenon thoroughly. Particle-in-cell (PIC) methods are widely used computational tools for this purpose.

The PIC method was introduced to the scientific community in the late 1950s [33] and it quickly became an integral part of plasma physics. The conceptual simplicity and efficient implementation on parallel supercomputers are only a few of the many reasons why the PIC algorithm is so popular.

2.1 PIC fundamentals

The PIC method belongs to particle simulations based on the kinetic approach. Meaning the system evolution is described via motion of charged particles, which have several conserved attributes (e.g., mass, charge) and variable attributes (e.g., position, velocity). The variable attributes evolve according to the equations of motion whose driving terms are given by the field equations [34]. However, real systems usually contain a huge amount of particles and it is simply impossible to describe every particle separately. Therefore it is necessary to reduce the description to just a statistical sample of particles [35].

The basic idea of the PIC method is to describe plasma using computational particles (so-called quasi- or macro-particles), which represent a group of real physical particles that are near each other in phase space. Although this approach significantly reduces the number of computational particles in simulation, the binary interactions for every pair in the system still cannot be taken into account [36]. Hence, instead of computing forces of interaction between every two particles, the PIC algorithm uses a computational grid to represent the mean values of the electric and magnetic fields, which are further used to calculate the force acting on computational particles. This approach is called the particle-mesh (P-M) method, whereas the second-mentioned is called the particle-particle (P-P) method. Using the P-M approach, we can significantly reduce the computing time, but at a cost of less accurate results. Although, this is usually not a complication for the interpretation of obtained results.

2.1.1   The Vlasov-Maxwell model

The Vlasov–Maxwell system of equations is used for the kinetic description of a collisionless plasma. In this approach, different species of particles constituting the plasma are described by their respective distribution functions $f_s(t, \vec{x}, \vec{p})$, where s denotes a given species consisting of particles with charge q_s and mass m_s, and $\vec{x}$ and $\vec{p}$ denote the position and momentum of a phase-space element [37]. The distribution function $f_s(t, \vec{x}, \vec{p})$ satisfies Vlasov's equation:

$$\frac{\partial f_s}{\partial t} + \frac{\vec{p}}{m_s \gamma} \cdot \nabla f_s + \vec{F}_L \cdot \nabla_s f_s = 0, \tag{2.1}$$

where γ is the relativistic Lorentz factor and

$$\vec{F}_L = q_s(\vec{E} + \vec{v} \times \vec{B}) \tag{2.2}$$

is the Lorentz force acting on a particle with velocity

$$\vec{v} = \frac{\vec{p}}{(m_s \gamma)}. \tag{2.3}$$

This force arises as a consequence of existence of collective electric $\vec{E}(t, \vec{x})$ and magnetic $\vec{B}(t, \vec{x})$ fields satisfying Maxwell's equations:

$$\nabla \times \vec{E} = -\frac{\partial \vec{B}}{\partial t}, \tag{2.4a}$$

$$\nabla \times \vec{B} = \mu_0 \varepsilon_0 \frac{\partial \vec{E}}{\partial t} + \mu_0 \vec{J}, \tag{2.4b}$$

$$\nabla \cdot \vec{E} = \frac{\rho}{\varepsilon_0}, \tag{2.4c}$$

$$\nabla \cdot \vec{B} = 0, \tag{2.4d}$$

where ε_0 and μ_0 are the vacuum permitivity and permeability, respectively. Equations (2.1) - (2.4), describing the dynamics of plasma, are called the Vlasov-Maxwell system of equations.

The electric and magnetic fields evolve according to the time-dependent equations (2.4a) and (2.4b), where the source term is in the form of the current density $\vec{j}$, which is produced by the motion of charged particles [38]. Combining the divergence of the equation (2.4b) and the time derivative of the equation(2.4c), one obtains the continuity equation:

$$\frac{\partial \rho}{\partial t} + \nabla \cdot \vec{J} = 0. \tag{2.5}$$

If the continuity equation is satisfied, then the equation (2.4c) is satisfied automatically during the system evolution, if it was valid at the beginning. As there is no magnetic charge the equation (2.4d) also remains valid if it was satisfied initially [38]. As a consequence, we may consider the divergence equation (2.4c) and (2.4d) as initial conditions only and our problem is reduced to solving the evolution equations (2.4a) and (2.4b).

2.1.2   Macro-particles

The mathematical formulation of the PIC method is obtained by assuming that the distribution function of each species is given by the sum of distribution functions for macro-particles $f_p(t, \vec{x}, \vec{p})$ [39]:

$$f_s(t, \vec{x}, \vec{p}) = \sum_p f_p(t, \vec{x}, \vec{p}). \tag{2.6}$$

The distribution function for each macro-particle can further be written as:

$$f_p(t, \vec{x}, \vec{p}) = w_p S_x(\vec{x} - \vec{x}_p(t)) S_p(\vec{p} - \vec{p}_p(t)), \tag{2.7}$$

where $S_x(\vec{x} - \vec{x}_p(t))$ and $S_p(\vec{p} - \vec{p}_p(t))$ are shape functions for the spatial and momentum coordinate respectively, and w_p is so-called particle weight (a term depending on the number of physical particles represented by each macro-particle).

There are several particular requirements for shape functions that need to be fulfilled [39]:

1. The support of the shape function is compact: $\exists R > 0$, supp $S_\xi \subset (-R, R)$.

2. Integral of the shape function is unitary: $\int_{-\infty}^{\infty} S_\xi(\xi - \xi_p)\, \mathrm{d}\xi = 1$.

3. The shape function is symmetrical: $S_\xi(\xi - \xi_p) = S_\xi(\xi_p - \xi)$.

Although these conditions are not very restrictive and therefore leave a wide range of options for selecting the shape functions, those used in practice are very few. As S_v is usually selected the Dirac delta function, the main advantage of this option is, that if all particles described by one computational particle have the same speed, they remain closer in the phase space during the subsequent evolution.

The conventional choice for shape function in space coordinate S_x are so-called b-splines. B-spline functions are a series of consecutively higher-order functions obtained from each other by integration [39]. The b-spline of zero degree $b_0(\xi)$ is a simple flat-top function defined as:

$$b_0(\xi) = \begin{cases} 1 & \text{if } |\xi| < \frac{1}{2} \\ 0 & \text{otherwise.} \end{cases} \tag{2.8}$$

B-splines of higher orders $b_l(\xi)$ can be obtained by integration using following formula:

$$b_l(\xi) = \int_{-\infty}^{\infty} b_0(\xi - \xi')b_{l-1}(\xi')\mathrm{d}\xi'. \tag{2.9}$$

The form of spatial shape function based on the b-splines in 1D is as follows:

$$S_x(x - x_p) = \frac{1}{\Delta_p} b_l\left(\frac{x - x_p}{\Delta_p}\right). \tag{2.10}$$

where Δ_p is the scale-length of the support of the computational particles (i.e. its size). The majority of PIC codes uses b-splines of the first or second degree. Usage of b-splines of higher order lowers the noise in the simulation, but at a cost of higher computational time.

2.1.3 Space discretization

In the PIC algorithm, Maxwell's equations in the time domain are solved using the Finite Difference Time Domain (FDTD) method. This approach is very popular for solving electromagnetic problems because it is quite simple to implement and more importantly, very effective and versatile. The FDTD method will be described in detail later in this chapter. For now, only the space discretization will be depicted, as it will be useful for describing the PIC algorithm.
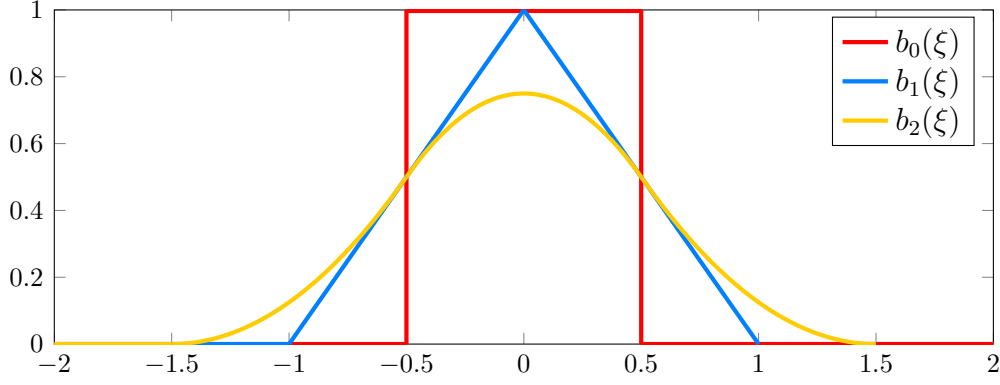
Figure 2.1: First three b-spline functions.

The electromagnetic fields are discretized onto a staggered spatial mesh, called the Yee-grid (fig. 2.2), as follows [40]:

$$\vec{E}_{ijk}^{(n)} \rightarrow \left[(E_x)_{i+\frac{1}{2},j,k}^n, (E_y)_{i,j+\frac{1}{2},k}^n, (E_z)_{i,j,k+\frac{1}{2}}^n \right] \tag{2.11}$$

$$\vec{B}_{ijk}^{(n)} \rightarrow \left[(B_x)_{i,j+\frac{1}{2},k+\frac{1}{2}}^{(n)}, (B_y)_{i+\frac{1}{2},j,k+\frac{1}{2}}^{(n)}, (B_z)_{i+\frac{1}{2},j+\frac{1}{2},k}^{(n)} \right] \tag{2.12}$$

Components of the current density $\vec{J}_{i,j,k}^n$ are defined in the same way as the components of $\vec{E}_{ijk}^n$, the charge ρ_{ijk}^n is defined in the corner of the cell:
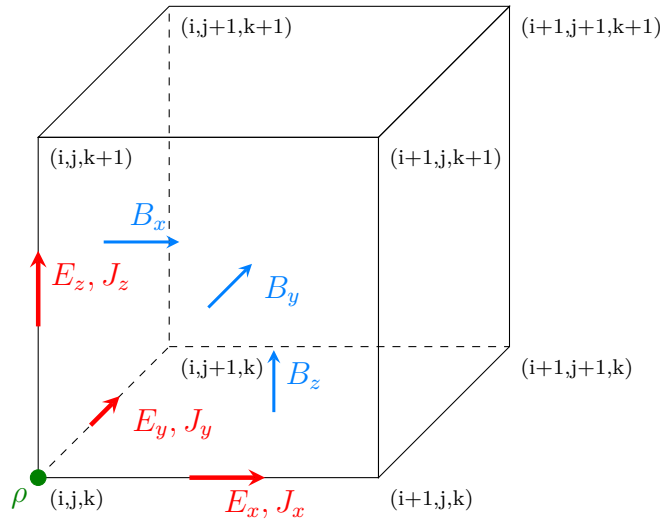
$$\vec{J}_{ijk}^{(n)} \rightarrow \left[(J_x)_{i+\frac{1}{2},j,k}^n, (J_y)_{i,j+\frac{1}{2},k}^n, (J_z)_{i,j,k+\frac{1}{2}}^n \right] \tag{2.13}$$

$$\rho_{ijk}^{(n)} \rightarrow \rho_{i,j,k}^n \tag{2.14}$$

Figure 2.2: Standard Cartesian Yee cell used for FDTD method

2.2   Particle-in-cell algorithm

The computational cycle of the PIC method can be divided into four main steps, which are shown in the fig. 2.3. First, the computational domain is discretized into a simulation mesh. At each time step, we use the position of the macro-particle (properties belonging to the macro-particles are labeled with subscript p) to determine the charge density. In the next step, we use this to compute the electromagnetic fields at the spatial grid (at discrete points marked with subscript (i,j,k)). Finally, the electromagnetic field is used to update particle velocities according to the Lorentz force. The new velocity is used to push particles to new positions and the whole process repeats [36].
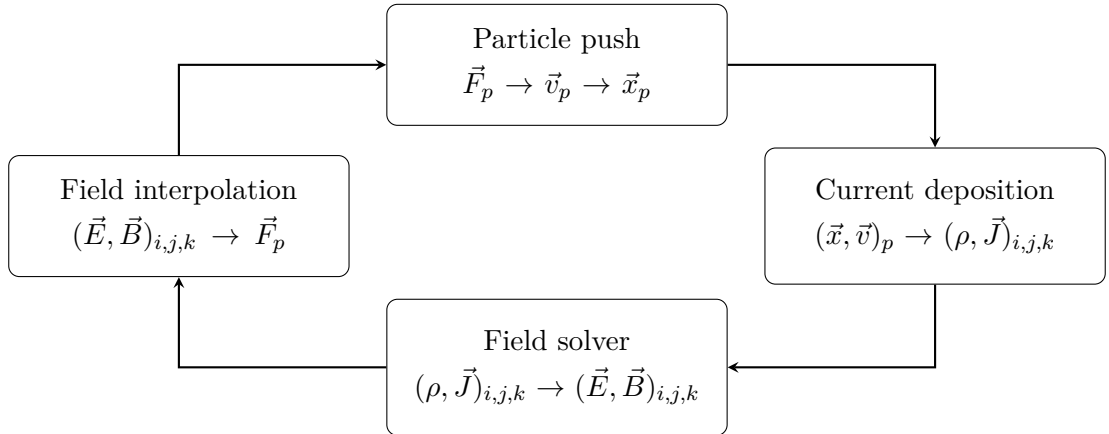
Figure 2.3: Computational cycle of the particle-in-cell method.

2.2.1   Initialization

The initialization of a PIC simulation is basically a three-step process consisting in: (i) creating particles, (ii) computing the initial total charge and current densities onto the grid, and (iii) solving the Poisson's equation to obtain the electrostatic field. It is also possible to add a fourth step - adding user defined external field (provided that its divergence is zero).

Usually the initial values (e.g. spatial profiles for the number density, the number of particle per cell, the mean velocity and the temperature of each species) are loaded from an input file defined by the user, but a lot of codes offers also a possibility to perform this step as a restart of a previous simulation. In this case the aforementioned values are directly copied from a file generated at the end of a previous simulation) [37].

2.2.2   Particle push

During PIC simulation the trajectory of all particles is followed in continuous phase space, this requires the solution of the equations of motion for each of them. This part of the code is frequently called "particle pusher" [41]. Since the particles can reach velocities near the speed of light, the relativistic case needs to be taken into account. If we denote:

$$\vec{u}_p = \gamma \vec{v}_p, \tag{2.15}$$

then the relativistic equations of motion to be solved are as follows:

$$\frac{d\vec{x}_p}{dt} = \frac{d\vec{u}_p}{\gamma} \tag{2.16}$$

$$\frac{d\vec{u}_p}{dt} = \frac{q_s}{m_s}\left(\vec{E}_p + \frac{\vec{u}_p}{\gamma_p} \times \vec{B}_p\right) = \frac{\vec{F}_p}{m_s}, \tag{2.17}$$

where $\vec{x}_p$ and $\vec{u}_p$ is macro-particle position and velocity and $\vec{F}_p$ represents a spatial average of the force acting on the macro-particle.

Differential equations (2.16) and (2.17) are integrated using the leap frog method, which is a second-order method and will be described in the next paragraph. The leap-frog algorithm is based on staggering the time levels of the velocity and position by half time step [39], so the macro-particle position is computed at the time level t^n and the velocity at $t^{n+\frac{1}{2}}$. To get position at time level $t^{n+1} = t^n + \Delta t$ need to use the velocity at mid-point $t^{n+\frac{1}{2}}$ and vice versa (see fig. 2.4).
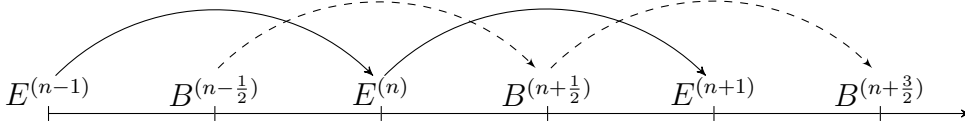
Figure 2.4: Visual representation of the leap-frog algorithm.

By applying this method to equations (2.16) and (2.17) and assuming, we know the electromagnetic fields at the position of each macro-particle, we obtain [37]:

$$\vec{x}_p^{(n+1)} = \vec{x}_p^{(n)} + \Delta t \frac{\vec{u}^{(n+\frac{1}{2})}}{\gamma_p^{(n+\frac{1}{2})}} \tag{2.18}$$

$$\vec{u}_p^{(n+\frac{1}{2})} = \vec{u}_p^{(n-\frac{1}{2})} + \Delta t \frac{q_s}{m_s}\left(\vec{E}_p^{(n)} + \frac{\vec{u}_p^{(n+\frac{1}{2})} + \vec{u}_p^{(n-\frac{1}{2})}}{2\gamma_p^{(n)}} \times \vec{B}_p^{(n)}\right). \tag{2.19}$$

The majority of PIC codes use the Boris method to solve equations (2.18) and (2.19), because it is capable of solving particle's dynamics accurately even for a large number of time-steps [42]. The Boris algorithm separates the effect of electric and magnetic fields by conveniently expressing terms for $\vec{u}_p^{(n+\frac{1}{2})}$ and $\vec{u}_p^{(n-\frac{1}{2})}$ as:

$$\vec{u}_p^{(n+\frac{1}{2})} = \vec{u}_p^{+} + \frac{q_s \vec{E}_p^{(n)}}{m_s}\frac{\Delta t}{2}, \qquad \vec{u}_p^{(n-\frac{1}{2})} = \vec{u}_p^{-} - \frac{q_s \vec{E}_p^{(n)}}{m_s}\frac{\Delta t}{2}. \tag{2.20}$$

Substituting 2.20 into 2.19 the electric field cancels:

$$\frac{\vec{u}_p^{+} - \vec{u}_p^{-}}{\Delta t} = \frac{q_s}{2m_s}(\vec{u}_p^{+} + \vec{u}_p^{-}) \times \vec{B}_p^{(n)}. \tag{2.21}$$

2.2.3   Charge and current density deposition

In the second step of the computational loop, usually referred as particle weighting, the charge and current densities are assigned from the position of macro-particles to the discrete grid points. These terms, given by:

$$\rho(t, \vec{x}) = \sum_s q_s \int f_s(t, \vec{x}, \vec{p})\mathrm{d}\vec{p} \tag{2.22}$$

$$\vec{J}(t, \vec{x}) = \sum_s q_s \int \vec{v} \cdot f_s(t, \vec{x}, \vec{p}) \mathrm{d}\vec{p} \tag{2.23}$$

will be later used to solve Maxwell equations. The charge and current density projection onto the grid is performed using the charge-conserving algorithm proposed by Esirkepov [43]. Considering the expression for macro-particle distribution function (2.7) it is possible to obtain following discretization of equations (2.22) and (2.23) [37]:

$$\rho_{i,j,k}^{(n)} = q_s w_p S_x(\vec{x}_{i,j,k} - \vec{x}_p), \tag{2.24}$$

$$(\vec{J}_{x,p})_{i+\frac{1}{2},j,k}^{(n+\frac{1}{2})} = (\vec{J}_{x,p})_{i-\frac{1}{2},j,k}^{(n+\frac{1}{2})} + q_s w_p \frac{\Delta x}{\Delta t} (W_x)_{i+\frac{1}{2},j,k}^{(n+\frac{1}{2})}. \tag{2.25}$$

Here $(W_x)^{(n+\frac{1}{2})}$ is a quantity computed from the particle current and former positions x_p^{n+1} and x_p^n using the method developed by Esirkepov [37]. Let us note that only the equation for x-component of vector $\vec{J}$ is given above, however, equations for y- and z-components would be analogous.

The deposited charge density is calculated only if required e.g. for diagnostic purposes. The reason is that charge densities are not needed to advance the electromagnetic fields, which will be shown in the next section.

2.2.4 Field solver

The next step is to advance electromagnetic fields in time according to Maxwell's equations using the deposited current as source term. Hence, we need to solve following equations:

$$\frac{\partial \vec{E}}{\partial t} = \nabla' \times \vec{B} - \vec{J}, \tag{2.26}$$

$$\frac{\partial \vec{B}}{\partial t} = -\nabla' \times \vec{E}, \tag{2.27}$$

where ∇' is the curl operators discretized using finite differences. The remaining divergence Maxwell's equations can be considered as initial conditions (if the continuity equation is fulfilled), hence, it is not necessary to solve them in this step.

To solve equations (2.26) and (2.27) the FDTD method is used. The continuous derivatives in space and time are approximated using a second-order accurate, two-point centered difference forms. Fields are staggered in space according to fig.2.2 and in time as follows: $\vec{E}$ is defined at times t^n, $\vec{B}$ and $\vec{J}$ are defined at times $t^{n+\frac{1}{2}}$.

For advancing the fields in time, the leap-frog scheme is used, which was described earlier. Therefore, the discretized equations (2.26) and (2.27) have the following form:

$$\frac{\vec{E}^{(n+1)} - \vec{E}^{(n)}}{\Delta t} = \nabla' \times \vec{B}^{(n+\frac{1}{2})} - \vec{J}^{(n+\frac{1}{2})}, \tag{2.28}$$

$$\frac{\vec{B}^{(n+\frac{1}{2})} - B^{(n-\frac{1}{2})}}{\Delta t} = -\nabla' \times \vec{E}^{(n)}. \tag{2.29}$$

To give a concrete example, considering the discrete form of the curl operator, the time derivative of E_x can be written as:

$$\frac{(E_x)_{i+\frac{1}{2},j,k}^{(n+1)} - (E_x)_{i+\frac{1}{2},j,k}^{(n)}}{\Delta t} = (J_x)_{i+\frac{1}{2},j,k}^{(n+\frac{1}{2})} + (\partial_y B_z)_{i+\frac{1}{2},j,k}^{(n+\frac{1}{2})} - (\partial_z B_y)_{i+\frac{1}{2},j,k}^{(n+\frac{1}{2})}, \tag{2.30}$$

where the partial derivatives in space are discretized as follows:

$$(\partial_x F)_{i,j,k} = \frac{F_{i+\frac{1}{2},j,k} - F_{i-\frac{1}{2},j,k}}{\Delta x}, \tag{2.31}$$

and corresponds to the usual curl-operator discretization used in the FDTD method. The definition for partial derivatives in y and z dimension are analogous.

2.2.5 Field interpolation

At this step of the loop, the fields acting on the macro-particles are computed. Using the electromagnetic field known at the discrete points (in the cells), we obtain the acting field for each particle p as:

$$\vec{E}_p^{(n)} = \int \vec{E}^{(n)}(\vec{x}) S_x(\vec{x} - \vec{x}_p^{(n)}) \mathrm{d}\vec{x}, \tag{2.32}$$

$$\vec{B}_p^{(n)} = \int \vec{B}^{(n)}(\vec{x}) S_x(\vec{x} - \vec{x}_p^{(n)}) \mathrm{d}\vec{x}, \tag{2.33}$$

where $\vec{E}^{(n)}$ and $\vec{B}^{(n)}$ are the cell averaged values of electric and magnetic fields. The interpolated fields at the macro-particle position can be calculated as:

$$\vec{E}_p^{(n)} = \sum_{i,j,k} \vec{E}_{i,j,k}^{(n)} S_x(\vec{x} - \vec{x}_p^{(n)}), \tag{2.34}$$

$$\vec{B}_p^{(n)} = \sum_{i,j,k} \vec{B}_{i,j,k}^{(n)} S_x(\vec{x} - \vec{x}_p^{(n)}). \tag{2.35}$$

For computing the macro-particle position later in the next step, we need the above mentioned time-centered magnetic fields $\vec{B}^{(n)}$, which is easily obtained from $\vec{B}^{(n+\frac{1}{2})}$ and $\vec{B}^{(n-\frac{1}{2})}$ as:

$$\vec{B}^{(n)} = \frac{1}{2}[\vec{B}^{(n+\frac{1}{2})} + \vec{B}^{(n-\frac{1}{2})}]. \tag{2.36}$$

2.3 Numerical stability and accuracy of the algorithm

Knowledge of stability conditions is crucial for all numerical methods. In PIC codes, stability of the simulation depends directly on the size of the time step Δt and spatial step Δx, i.e. the cell size, hence, also Δy and Δz in multidimensional simulations. In most cases, all spatial steps can have the same size. However, in highly computationally demanding simulations cell size in directions transverse to the laser propagation tends to be larger to limit the overall number of cells.

Since the PIC codes are usually very robust numerical stability itself does not guarantee physically correct results. Therefore, the choice of the cell size is heavily influenced by the investigated physical phenomena. In many cases, we need to successfully unravel of the physical phenomenons at plasma-vacuum boundary. Hence the spatial step in the direction of large density gradient is limited by the plasma skin depth [44]:

$$\Delta x \leq \frac{c}{\omega_{pe}}. \tag{2.37}$$

In the general electromagnetic case, the time step δt limited by Courant-Friedrichs-Lewy (CFL) condition required for stable propagation of electromagnetic waves [45]:

$$C = c^2 \Delta t^2 \left(\frac{1}{\Delta x^2} + \frac{1}{\Delta y^2} + \frac{1}{\Delta z^2} \right), \tag{2.38}$$

where C is the CFL number ($0 < C < 1$). This condition ensures that macroparticles can not move further than one cell per time step, otherwise the calculation of currents would be inaccurate and the growth of non-physical effects can be quite rapid.

The second condition for the time step emerge from the requirement to resolve all important frequencies (according to the Nyquist-Shannon theorem) [46]:

$$\omega_m \Delta t \leq 2. \tag{2.39}$$

2.4 Used PIC codes

Simulations for the master's thesis were performed using two different codes - first was an open-source, high-performance, and multi-purpose PIC code called Smilei (for "Simulating Matter Irradiated by Light at Extreme Intensities") developed in France as a joint effort between scientists from CEA (Alternative Energies and Atomic Energy Commission), CNRS (Centre national de la recherche scientifique) and two universities (Université Paris-Saclay and Université Versailles Saint-Quentin). The second code is called WarpX, also an open-source, which supports many features including mesh refinement and the boosted-frame technique. WarpX was developed at UC Berkeley and Lawrence Berkeley National Laboratory.

Both codes offers advanced numerical techniques (e.g. azimuthal modes decompositions or Perfectly-Matched Layers boundary conditions) and various additional physics modules (e.g. field ionization or binary collisions). Codes are able to cover a wide range of physical problems, from astrophysics to relativistic laser-plasma interaction, which is also the topic of this research project.

2.4.1 Smilei

The parameters for simulation are set using an input file, which is called namelist and it is written in Python. It is possible to control various aspects of the simulation, for example, the number of grid points in the simulation domain (in particular directions), particle shape function, or the initial distribution of particles. The code also allows running simulations in one, two, and three dimensions and to choose between various Maxwell solvers, particle pushers, etc.

Like many PIC codes, Smilei handles only dimension-less variables, normalized to reference quantities [37]. It is convenient to use the speed of light c, the elementary charge e, and the electron mass m_e as a basis of the normalizations. A summary of the arbitrary reference quantities used in Smilei, is given in the Appendix. The scale of the problem is not decided a priori, and the user is free to scale the result of the simulation to any value based on an unknown reference frequency ω_r. Usually, it will be an important frequency of the problem (for example, the electron plasma frequency or angular laser frequency). It is worth mentioning that for simulating ionization or collisions ω_r needs to be defined in the namelist, in SI units.

Smilei has its own module for post-processing called happi, which can be directly imported to Python. Hence, apart from several methods for finding information

on the namelist and opening various diagnostics, all of the Python packages like
NumPy or Matplotlib are also available for processing the results.

To ensure the versatility of the code, Smilei is written in C++ and based on
an object-oriented architecture. It was co-developed by both physicists and HPC ex-
perts to best benefit from the new high-performance computing (HPC) architectures.
The main computational features include dynamic load balancing and state-of-the-
art hybrid MPI/OpenMP parallelization simple instruction multiple data (SIMD)
vectorization.

2.4.2   WarpX

The input parameters for WarpX are basically the same as for Smilei (or any other
PIC code), however, they are defined in a simple text file. This makes writing the
input file a little bit less versatile nonetheless, the code uses PICMI (The Particle-In-
Cell Modeling Interface) standard, which allows writing input files also using Python
and then converting them into suitable format for WarpX. Another difference from
Smilei is that WarpX operates in SI units.

WarpX is very versatile in regard to post-processing. The code offers different for-
mats for output data (plotfile (AMReX) or openPMD formats like HDF5 or ADIOS)
which can be further visualized using variable Python based software or ParaView.
In addition, WarpX also has in-situ visualization capabilities (i.e. visualizing the
data directly from the simulation, without dumping data files to disk).

WarpX is highly-parallel and highly-optimized code, running on GPUs and multi-
core CPUs written in C++ and designed for high-performance on the world's largest
supercomputers. In addition, WarpX is also a multi-platform code (running on
Linux, macOS or Windows) and was awarded the ACM Gordon Bell Prize in 2022.

Chapter 3

Advanced numerical techniques in PIC simulations

The process of laser-plasma acceleration inherently includes strongly nonlinear phenomena, which are intrinsically three-dimensional and cannot be appropriately described using 1D or 2D geometries. These phenomena include e.g. pulse self-focusing and beam loading. Moreover, determining, for example, the beam charge from a 2-D simulation is very tricky, since the macroparticles are represented as infinite lines instead of spheres.

These problems become even more severe while modeling the laser interaction with solid objects, e.g. a nanoparticle (as is the case of this thesis), which is in 2-D represented as a wire. Consequently, even if the whole problem is cylindrically symmetrical, the properties of the accelerated electron bunch obtained from 2-D simulations can significantly differ depending on whether the laser polarization is parallel or perpendicular to the "wire". Hence, performing 3-D simulations is absolutely necessary for designing a nanoparticle gas target and for a proper understanding of the processes involved during the electron injection.

However, 3-D PIC simulations demand extreme computer resources and can be challenging even for current supercomputers. As a first step to reduce the overall computational cost, it is standard for PIC simulations of the LWFA process to use a so-called moving window to follow the laser driver, the wake, and the accelerated beam. The simulation domain moves at a constant speed (close to the speed of light) which means that particles are removed from the left-hand edge of the domain and new particles are introduced at the right-hand edge (assuming that the laser pulse propagates from the left to the right) [47]. This results in huge savings, by avoiding the meshing of the entire plasma that is orders of magnitude longer than the other length scales of interest.

Most high-performance PIC codes have also implemented some advanced techniques that may help significantly reduce the simulation run time. Nonetheless, it is necessary to know which assumptions were made during the implementation and therefore, whether a particular numerical technique can be used for our purposes.

In this chapter, some of the common means to make 3-D PIC simulations less computationally expensive will be briefly discussed. More emphasis will be on two particular techniques, namely azimuthal modes (AM) decomposition (sometimes called quasi-3D approach) and mesh refinement, which is suitable for simulations of the electron acceleration using nanoparticle gas targets.

3.1　Azimuthal modes decomposition

This approach is suitable for systems with (or close to) cylindrical symmetry, which is quite common for LWFA. In this case, the three-dimensional description is achieved using cylindrical geometry and Fourier decomposition of the electromagnetic fields along the azimuthal coordinate θ hence, the azimuthal modes decomposition. The cost of such simulation is approximately m-times the cost of 2-D simulation where m is the number of used modes.

Note that the AM decomposition concerns only the grid quantities (i.e. electromagnetic fields and current densities), which are defined on a 2D grid. However macro-particles evolve in a 3-D space described by cartesian geometry (using reconstructed 3D cartesian electromagnetic fields) [48]. Simulations, which are using this method, are frequently referred to as quasi-3D simulations.
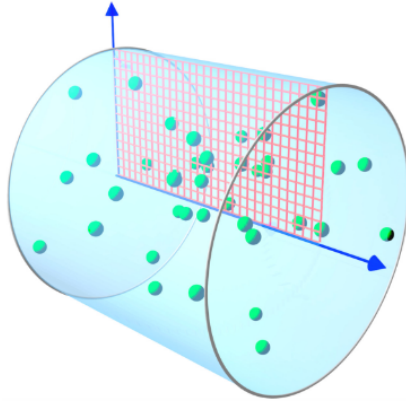
Figure 3.1: Schematic picture of the geometry of an AM decomposition computational domain; (red) 2-D grid where the electromagnetic fields are defined, (green dots) macroparticles defined in 3-D [48].

3.1.1　Mathematical description

At first, to decompose vector fields in azimuthal modes one needs to express their components along the cylindrical coordinates $(\vec{e}_z, \vec{e}_r, \vec{e}_\theta)$. For example, the transverse field of a laser pulse linearly polarized in the $\vec{y}$ direction with a cylindrically symmetric envelope can be written as:

$$\vec{E}(r, z, \theta, t) = E_y(r, z, \theta, t)\vec{e}_y = E_y(r, z, t)\Big(\cos(\theta)\vec{e}_r - \sin(\theta)e_\theta\Big). \qquad (3.1)$$

Here $E_y(r, z, \theta, t)$ is now a scalar field, whereas any scalar field $F(r, z, \theta, t)$ can be represent as a sum of azimuthal modes, using Fourier decomposition along θ:

$$F(r, z, \theta, t) = \Re\left(\sum_{m=0}^{+\infty} \tilde{F}^m(r, z)e^{-im\theta} \right), \qquad (3.2)$$

where m is the number of the mode and $\tilde{F}^m$ is the Fourier coefficient. An infinite expansion sum is by all means not suitable for numerical calculations hence, we assume that only the first N_m modes are important (i.e. the higher modes are omitted).

$$F(r, z, \theta, t) = \Re\left(\sum_{m=0}^{N_m-1} \tilde{F}^m(r, z)e^{-im\theta} \right). \qquad (3.3)$$

As already mentioned, the AM decomposition is most suited for physical problems close to cylindrical symmetry as a low number of modes is sufficient. Note that expression (3.1) corresponds to the first order term ($m = 1$) in a Fourier expansion of the laser field. Similarly, an elliptically (or cylindrically) polarized laser can be described also using only mode $m = 1$, as it can be seen as the linear superposition of two linearly polarized lasers. Note the laser envelope needs to be cylindrically symmetrical, else higher modes are necessary (e.g. to get a laser beam with an elliptically shaped trace, one needs to use a minimum of three modes). However, in practice, for LWFA simulations only the first two or three orders are usually used.

In PIC codes the time evolution of electric and magnetic fields is obtained by solving time-dependent Maxwell's equations (2.4a, 2.4b). As these equations are linear, different Fourier modes evolve independently in the vacuum thus, can be solved independently for each mode. Naturally, in presence of the plasma, modes become coupled, for example, the laser pulse ($m = 1$) will create a plasma wave with corresponding wakefield ($m = 0$). However, the coupling between the modes manifests itself during the field interpolations step, i.e. when the total electromagnetic fields push the macro-particles. Hence, the evolution of fields is obtained by solving equations (2.4a, 2.4b) in cylindrical coordinates separately for each mode, for example, equation (2.4b) can be rewritten as:

$$\frac{\partial \tilde{E}_r^m}{\partial t} = \frac{im}{r}\tilde{B}_z^m + \frac{\partial \tilde{B}_\theta^m}{\partial z} - \tilde{J}_r^m, \tag{3.4a}$$

$$\frac{\partial \tilde{E}_\theta^m}{\partial t} = -\frac{\partial \tilde{B}_r^m}{\partial z} - \frac{\partial \tilde{B}_z^m}{\partial r} - \tilde{J}_\theta^m, \tag{3.4b}$$

$$\frac{\partial \tilde{E}_z^m}{\partial t} = -\frac{1}{r}\frac{\partial}{\partial r}(r\tilde{B}_\theta^m) - \frac{im}{r}\tilde{B}_r^m - \tilde{J}_z^m. \tag{3.4c}$$

Note that equation (2.4a) could be expressed equivalently and that we assumed that the densities and currents can also be decomposed in modes. Whereas, currents are calculated by projecting macro-particle velocities over the grid (r, z) and the Fourier modes. However, this algorithm is not charge conserving thus, to ensure the fulfillment of the Poisson equation a field E_c is added to the electric field. This correction field is obtained by solving the Poisson equation [49]:

$$\nabla \cdot \vec{E}_c = \rho - \nabla \cdot \vec{E}. \tag{3.5}$$

The rest of PIC loop runs as described in chapter 2.

3.2   Mesh refinement

Plasma simulations are frequently linked with challenges regarding the disparity of scales which must be resolved. An example is, for instance, detailed modeling of the beam behavior from end-to-end in a Heavy Ion Fusion accelerator [50]. However, in LWFA we seldom encounter this problem, because the main resolution requirements usually come from resolving the laser wavelength. On the other hand, it is possible one would like to have a finer mesh, for example, in the region of anticipated electron injection. In this thesis, we need to appropriately resolve the nanoparticle with a size under 100 nm, its ionization, and following electron injection, which requires better resolution than the rest of the simulation domain.

Above mentioned examples have one thing in common, that is mentioned disparities are in distinctive regions of the simulation domain. This issue can be solved by so-called mesh refinement (MR), a technique used for refining certain regions of the computational grid. This method serves as a "numerical microscope," allowing one to "zoom in" on the specific regions, that are most important to the solution of a particular problem [50]. Although mesh refinement has proven to be very effective and the approach is widely used in other areas of computational physics, e.g. computational fluid dynamics, it is not commonly used in PIC simulations. The reason is the rather challenging implementation of the MR to PIC algorithm.

The implementation of the MR technique to PIC simulations requires special care to avoid the introduction of spurious effects into the model, or at least to minimize them. As the two main generic issues were identified the spurious self-force on macroparticles close to the mesh refinement interface [50] and the reflection (and possible amplification) of short wavelength electromagnetic waves at the mesh refinement interface [51]. The reason is that a wavelength resolved on a region with finer mesh may not be described on a coarser grid, therefore, it is reflected on the interface. Such behavior is nonphysical and by multiple reflections on the boundaries, it can significantly increase the field energy, creating instability. Moreover, these waves may affect the particle motion, unless they are heavily damped inside the grid, or absorbed at the interface.

As a result, the implementation of the mesh refinement to a PIC code is quite challenging and complicated. Moreover, for reasons described in the next chapter we eventually decided not to run simulations using the mesh refinement technique. Therefore, this thesis will not provide a detailed description of the implementation of the mesh refinement technique. However, it can be find e.g. in [50], [52] or [53].

3.3 Additional numerical schemes

In this section, four additional numerical techniques designed to reduce the computational cost of 3-D PIC simulations will be described. The common denominator of these methods is an effort to lower the number of cells in the computational domain (i.e. get larger cells) to enable studying of very long propagation paths (cm-m). This kind of simulation is necessary to design accelerators obtaining electrons with GeV energies, which is out of reach using fully 3-D PIC simulations.

In LWFA simulations, the main restrictions for resolution usually come from the need to resolve laser wavelength. Thus, the following methods use either some approximations for quickly varying electromagnetic fields of laser oscillations (laser envelope model and quasi-static simulations) or a convenient transformation of coordinates.

3.3.1 Lorentz boosted frame

As the name of the method indicates, it is based on relativistic Lorentz transformation. Hence, the simulation is not calculated in a laboratory frame as usual, but in a frame of reference traveling close to the speed of light in the direction of the laser beam. As a result of well-known properties of the Lorentz transformation, i.e. the contraction and dilation of space and time, the fast and short laser driver beam elongates, while the stationary plasma is contracted. Hence, the inequality

between scales is reduced, and thereby the number of time steps to complete the simulation decrease by orders of magnitude (up to a few hundred [51]). Note this method does not make any approximations of the physics model.

However, this approach has also a few limitations. The first involves macroparticle statistics and emerges as a consequence of plasma being represented by fewer macroparticles in the boosted frame and it can cause issues e.g. for modeling of electron injection. The second one concerns backward-propagating waves, which are harder to resolve because the Lorentz transformation "shrinks" them (as opposed to forward propagating laser). This makes it impossible for boosted-frame simulations to model e.g. colliding pulse injection. Also, the speedup of simulations using this method is not sufficient to model acceleration stages leading to GeV electrons.
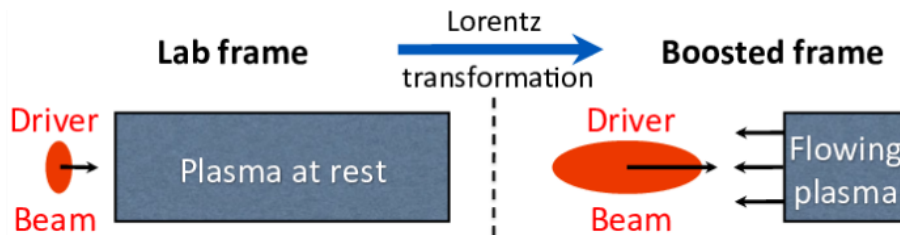
Figure 3.2: Schematic image of the effect of the Lorentz transformation on laser beam travelling close to the speed of light and plasma at rest [51].

3.3.2 Laser envelope model

Another method to substantially improve the performance of LWFA simulations is by modeling the evolution of the laser envelope rather than the rapidly oscillating field itself. Hence, one only needs to resolve the plasma wavelength λ_p and not the laser wavelength λ_L, which allows the coarsening of the grid, particularly in the direction of the laser propagation. Thus, fewer timesteps are required. The savings of computational resources correspond approximately to $(\lambda_p/\lambda_L)^2$ ($\approx$ three orders of magnitude) [54].

Some drawbacks of this method are its inability to describe self-injection or electron trapping in regions of strong laser field and the fact that laser oscillations may not be the only phenomena requiring high resolution (e.g. sharp bubble edges). Other complications may emerge while modeling the laser depletion, because the laser wavelength may change during depletion.

3.3.3 Quasi-static PIC codes

Codes using the quasi-static approximation (QSA) are particularly useful for studying very long propagation paths (cm-m). The QSA assumes that the laser pulse does not vary during the time a plasma electron needs to pass the pulse, hence the evolution of the beam and plasma is decoupled. Note this approximation also requires the assumption of a slowly evolving wakefield structure, thus neither the laser period nor the plasma period, need not be resolved in time. Under this approximation, the Maxwell equations take the form of the Poisson equation, and the scheme is no longer subject to a CFL condition [55]. This makes it possible to use time steps orders of magnitude larger than those in conventional electromagnetic PIC.

The main problem of quasi-static PIC codes is their inability to model the particle injection. On the other hand, they often enable consistent initialization of particle beams in the plasma. This is an important presumption towards running so-called hybrid PIC simulations [55], which is a way of simulating the whole acceleration process. A hybrid simulation is a combination of full 3-D PIC code, used for simulating the internal electron injection (length scale μm-mm), and a quasi-static PIC code, to model further propagation of the laser driver and electron beam after the injection process (length scale cm-m).

Chapter 4

Comparison of 3D and quasi-3D approach

The decision whether to choose an azimuthal modes decomposition (cylindrical geometry) or a full 3D simulation with mesh refinement, was made based on several factors. The main aspects taken into consideration were: the computational cost of a single simulation, differences in results obtained using these two approaches, and also achieved code performance since different PIC codes were used. In this chapter, a detailed comparison of both geometries is provided.

4.1   Computational cost and code performance

4.1.1   Computational cost

Computational cost of full 3D simulation, respectively quasi-cylindrical simulation, can be estimated as follows:

$$N_{comp,3D} \approx \left(\frac{L_x}{\Delta x}\right) \times \left(\frac{L_y}{\Delta y}\right) \times \left(\frac{L_z}{\Delta z}\right) \times \left(\frac{T_{sim}}{\Delta t}\right), \tag{4.1}$$

$$N_{comp,RZ} \approx \left(\frac{L_r}{\Delta r}\right) \times \left(\frac{L'_z}{\Delta z'}\right) \times \left(\frac{T'_{sim}}{\Delta t'}\right) \times M. \tag{4.2}$$

Here L_x, L_y, L_z, L'_z and L_r are the dimensions of the simulation domain, $\Delta x, \Delta y, \Delta z$, $\Delta z'$ and Δr are cell sizes in corresponding directions, T_{sim} is the simulation time, Δt and $\Delta t'$ are timesteps and $M = 2$ is the number of azimuthal modes used for the decomposition of electromagnetic fields.

Now, considering the use of mesh refinement in the 3D simulation and requirements for the stability of quasi-cylindrical simulation, it is possible to compare the computational cost of both considered approaches. For an identical simulation run in 3D and cylindrical geometry holds:

$$L_z = L'_z, \qquad L_x = L_y = 2L_r, \tag{4.3}$$

since in cylindrical geometry (as a result of cylindrical symmetry) is sufficient to use only half of the simulation domain in the radial direction.

Furthermore, the minimum cell size for resolving the nanoparticle with diameter d_{np} and its ionization is $\Delta_\parallel = d_{np}/4$ in the direction of the laser propagation and

$\Delta_\perp = d_{np}/2$ in the perpendicular direction. Considering the vast majority of cells can be (at least) twice as big while using the mesh refinement one can write:

$$\Delta x = \Delta y = 2\Delta r = \frac{\lambda}{10}, \qquad \Delta z = 4\Delta z' = \frac{\lambda}{20}. \tag{4.4}$$

The second condition is a consequence of the quasi-cylindrical simulation stability requirement for the cell size in the z-direction to be at least four times larger than the cell size in the radial direction. Although the resolution specifications would allow using even $\Delta x = \Delta y = 4\Delta r$, the maximum refinement ratio currently implemented in WarpX is only 2.

Finally, the relation between time variables for the respective simulation geometries is as follows:

$$T_{sim} = T'_{sim}, \qquad \Delta t \approx \frac{10}{3}\Delta t', \tag{4.5}$$

whereas the second relation was obtained combining equation (2.38) and (4.4). Now, one can determine the ratio between $N_{comp,3D}$ and $N_{comp,RZ}$:

$$\frac{N_{comp,3D}}{N_{comp,RZ}} \approx \frac{\left(\frac{L_x}{\Delta x}\right) \times \left(\frac{L_x}{\Delta x}\right) \times \left(\frac{L_z}{\Delta z}\right) \times \left(\frac{T_{sim}}{\Delta t}\right)}{\left(\frac{2L_x}{2\Delta x}\right) \times \left(\frac{4L_z}{\Delta z}\right) \times \left(\frac{T_{sim}}{\Delta t}\frac{10}{3}\right) \times 2} = \frac{3}{80}\left(\frac{L_x}{\Delta x}\right). \tag{4.6}$$

Therefore, the ratio between $N_{comp,3D}$ and $N_{comp,RZ}$ is directly dependent on the number of cells in the direction perpendicular to the direction of the laser propagation. Furthermore, considering $\Delta x = d_{np} \approx 100$ nm (before the mesh refinement) and L_x between 50 μm and 200 μm one can obtain an estimate:

$$\frac{N_{comp,3D}}{N_{comp,RZ}} \approx 20 - 75. \tag{4.7}$$

Thus, by choosing cylindrical geometry over full 3D simulation, one can save a significant amount of computational resources. Moreover, savings would be even higher for nanoparticles with smaller diameters. Note, that the considered resolution in every direction is also good enough to satisfy requirements for resolving laser wavelength about 1μm.

4.1.2 Code performance

The next criterion used to decide, whether to choose the full 3D or cylindrical geometry, was the difference in performance of the two considered PIC codes; Smilei and WarpX. Since we have already had certain experiences with Smilei, we known how to properly decompose the computational domain and how effectively perform the parallelization on a super computer.

However, the WarpX code was explored solely for the purpose of using the mesh refinement technique to resolve the nanoparticle, hence, we do not have any prior experiences with this PIC code. Hence, due to a lack of time, we were not able to determine a suitable domain decomposition and/or MPI parallelization to acquire a good code performance. Nevertheless, in the future, we would like to revisit this issue, possibly try using GPU nodes instead of CPU nodes and realize a full 3D (or quasi-cylindrical) simulation with mesh refinement to model the nanoparticle more effectively.

4.2 Results comparison

As already mentioned, using the AM decomposition and running a simulation in cylindrical geometry results in a significant reduction of the computational cost. However, a significant part of the scientific community is often skeptical about results acquired using the AM decomposition instead of full 3D PIC simulations. Hence, a couple of simulations were performed to compare the results obtained with both approaches.

For the sake of simplicity, and to avoid wasting computational time, simulations meant for the comparison of 3D and quasi-3D method are ran without the presence of a nanoparticle, hence, a coarser resolution is sufficient. Therefore, chosen cell size in direction of the laser propagation in full 3D simulation is 42.5 nm ($\lambda_0/20$), and 85 nm ($\lambda_0/10$)in the perpendicular direction. The size of the simulation domain is $55 \times 55 \times 55$ μm hence, there are approximately 640 cells in the transversal directions and 1300 cells in the longitudinal direction. In the cylindrical geometry, the cell size is 21.25 nm $\times$ 85 nm ($\lambda_0/40 \times \lambda_0/10$) and the simulation domain is 27.5×55 μm, yielding 320 cells in the r-direction and 2600 cells in the z-direction.

The laser parameters are as follows; the laser wavelength $\lambda_0 = 850$ nm, the focal spot is characterized by $d_{FWHM} = 3$ μm the pulse duration is t_{FWHM}= 15 fs (considering Gaussian profile in time and space). The energy contained in the pulse is 40 mJ, which corresponds to the intensity of 9.2×10^{18} W/cm^2 and $a_0 = 2.2$.

In this simulation, a 1 mm long gas target with double Gaussian shape and particle density 1.6×10^{19} cm^{-3} composed of nitrogen molecules was used. Note that only a part of the gas target was simulated as its plateau is only 200 μm wide and the wakefield quickly diminishes with decreasing gas density and weakening laser pulse. The total simulated length (using the moving window algorithm) is 680 μm, which corresponds to a simulation time of 2266 fs or 800 T_0 (T_0 is the laser period). The simulation timestep is chosen according to the CFL condition with $C = 0.95$.

In the case of the 3D simulation 4 particles per cell were used. Hence, the total amount of macro-particles in the computational domain was approximately 4×10^9. As for the simulation using cylindrical geometry, two azimuthal modes had to be used to model the linearly polarized laser pulse. Since simulations using the AM decomposition usually require more macro-particles to obtain a representative sample, 32 particles per cell were used. In total, this makes 1.3×10^7 particles in the computational domain. The 3D simulation requires approximately 17 000 timesteps, whereas the quasi-cylindrical simulation requires cca 35 000 timesteps.

4.2.1 Electron beam

In this subsection, the differences in properties of the generated electron beam will be addressed. First, notice the figure 4.1 depicting the energy spectra of the electron beams for different geometries. Qualitatively, these results are in very good agreement, the mean energy is approximately 20 MeV and the relative energy spread is around 17 %. The amount of injected electrons is approximately twice as high in the quasi-cylindrical simulation than in the case of 3D geometry. This quantity is directly connected with electron beam charge, which can consequently differ in different simulation geometries.

However, this should not be a crucial obstacle, since the results differ only slightly and we can take this fact into account. Regardless, it cannot be expected to obtain

exactly the same results from experiments and numerical simulations. Hence, to get an estimate of the most suitable gas target parameters, the quasi-cylindrical simulation seems to be a viable option.
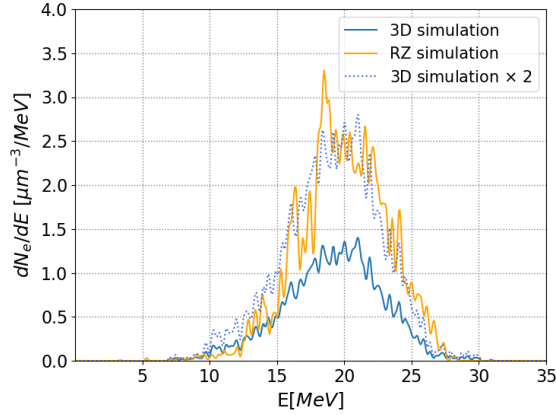
Figure 4.1: Comparison of electron energy spectra obtained from 3D and quasi-cylindrical simulation. Note the electron beam energy and energy spread are in a good agreement although the amount of injected electrons is lower in the case of 3D simulation.

Apart from the energy spectrum, it is useful to also examine the spatial profile of the accelerated electron beam, results from both simulations is depicted in fig. 4.2. Similar to the energy spectrum a good resemblance was obtained, there is only one generated electron beam, whereas the beam diameter is approximately 15 μm. The only notable differences are in the amount of injected electrons in the z-direction (the left picture in fig. 4.2) and in the number of electrons farther from the center of the computational domain in x-direction, which is slightly higher in the 3D geometry (middle picture in fig. 4.2).
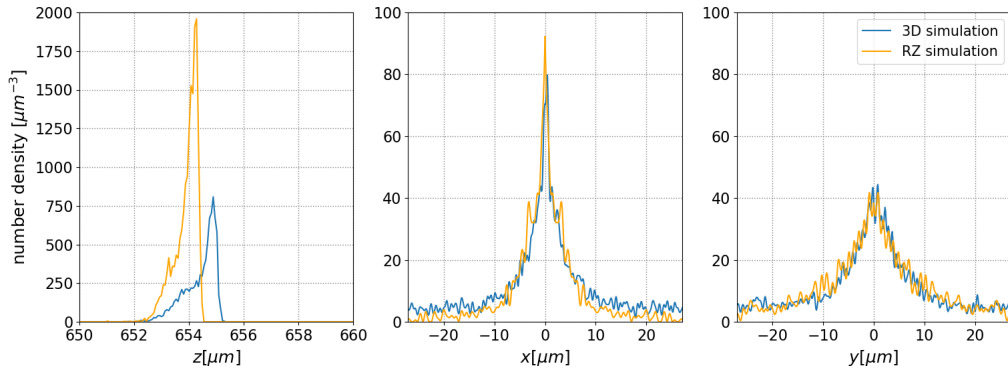
Figure 4.2: Electron beam profiles in longitudinal and transversal directions from 3D (blue line) and quasi-cylindrical (orange line) simulation. In left picture, a longitudinal profile is depicted. In this case the number of electrons obtained from the quasi-cylindrical simulation is approximately twice as high compared to the 3D simulation. The center and right picture display the transversal profiles. Both simulations give almost identical results.

Finally, one more set of plots (fig. 4.3), related to the electron beam longitudinal phase space, is presented. This quantity follows the same trend as previous results, both simulations are in good agreement qualitatively, but the amount of electrons obtained from quasi-cylindrical simulation is higher than from 3D simulation. One can also notice the beam from the quasi-cylindrical simulations occupies a smaller

area in the longitudinal phase space and has higher share of electrons with higher energy.

(a)

(b)
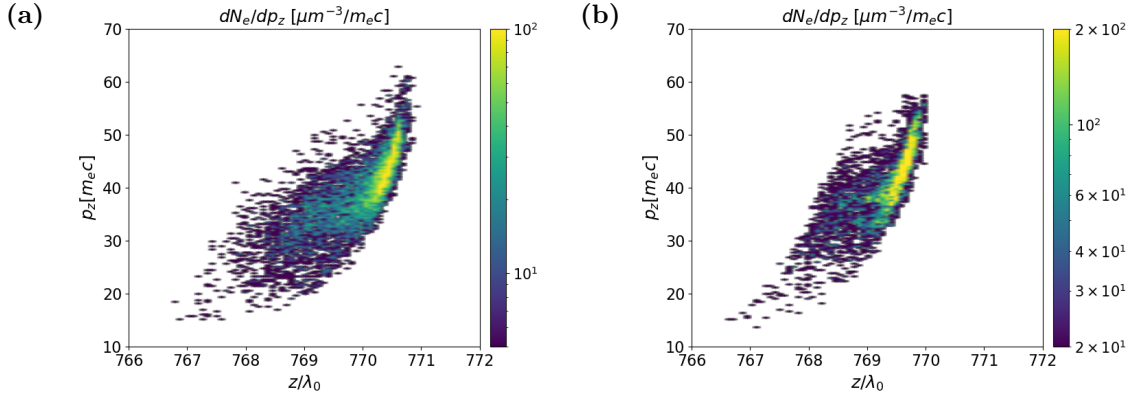
Figure 4.3: Longitudinal phase space of electrons obtained from (a) 3D and (b) quasi-cylindrical simulation. Note the scales are logarithmic and saturated to ensure a good contrast.

4.2.2 Wakefield and electron density

The second part of the comparison of the results is dedicated to the distribution of fields, which is depicted in fig. 4.4. For the analysis, only the area of the gas target plateau was chosen. This region was chosen because the laser pulse has a short Rayleigh length. Hence, its intensity rapidly decreases as the laser pulse quickly diverges farther from its focus. Consequently, the wakefield weakens and perturbations in the electron density are less distinctive. Thus, it is difficult to compare results from respective simulations, because plots do not contain any characteristic details. Moreover, these regions have a rather minor influence on the acceleration process, since the electron injection takes place in the gas target plateau and as the the wakefield weakens it is no longer able to accelerate injected electrons.

Therefore, figure 4.4 depicts the driving laser pulse (green), electron density distribution (grey), and the profile of the plasma wave longitudinal electric field (orange line) at $x \approx 0$. This choice was made on the fact that in quasi-cylindrical simulations there is usually quite a strong noise present at the simulations axis. This can be observed e.g. on fig. 4.4(b) or (d).

First, discrepancies in the electron density distribution at different times will be described. Every pair of plots differs solely in minor details, while the most important characteristics are almost identical. Most differences can be spotted comparing cases (a) and (b). For example, in the picture from the 3D simulation (case (a)), the edge of the first bubble is sharper and the shape of the second bubble is slightly different than in case (b). Furthermore, in the majority of cases one can spot lower electron density (especially farther from the center of the computational domain) in the case of 3D simulations. Between cases (e),(f), and (g),(h) no other notable differences were found. Moreover, profiles of the longitudinal electric field, as well as their amplitude, are also in good agreement.

To sum up, results from simulations using 3D and cylindrical geometry, are overall in good agreement. Hence, for designing a gas target for an LWFA experiment, quasi-3D simulations based on AM decomposition, are a great compromise between inaccurate 2D simulations and costly full 3D simulations.
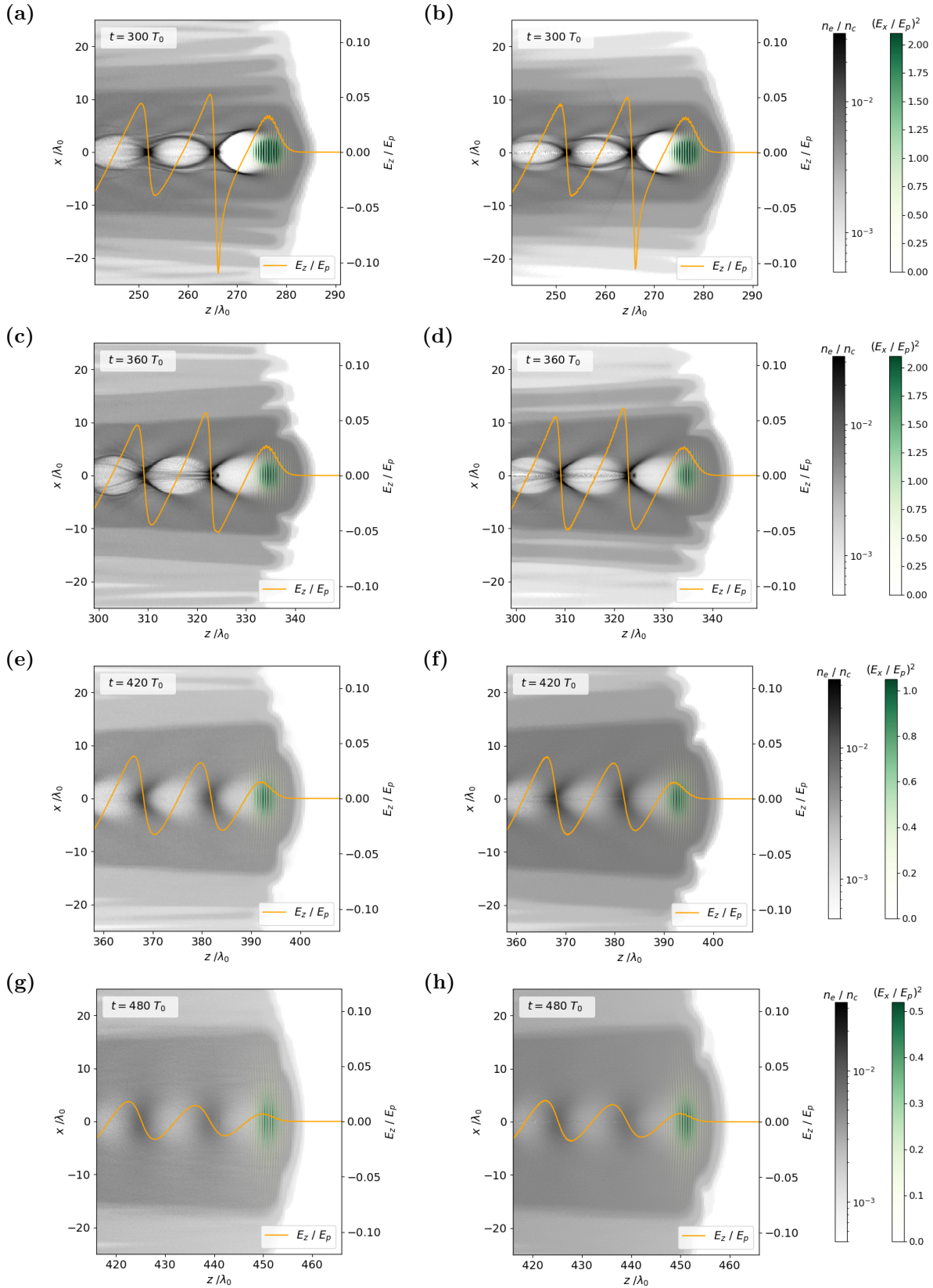
Figure 4.4: Electron density distribution obtained from 3D (left column) and quasi-cylindrical simulation (right column). The plots are plotted at following times (a,b) t = 300 T_0, (c,d) t = 360 T_0, (e,f) t = 420 T_0 and (g,h) t = 480 T_0. The color scales are saturated and in case of electron density also logarithmic. Note, that the profile of the electric field is not plotted exactly at $x = 0$ since there is a lot of noise at the axis, instead it is plotted two cells below the axis.

Chapter 5

Simulations for study of nanoparticle electron injection

For the parametric study of the nanoparticle influence on the electron injection and accelerated electron beam, several PIC simulations in cylindrical geometry (quasi-3D approach) were carried out using open-source PIC code Smilei [48]. Since we would like to perform an experiment using the nanoparticle injection scheme in the future, two different gas targets (approximately 1 mm and 20 mm long) affiliated with two particular experiments ALFA (Allegra Laser For Acceleration) and ELBA (ELectron Beam Accelerator for fundamental sciences and applications) at ELI Beamlines were chosen. The goal was to determine whether this injection scheme is suitable for these experiments and if so, try to find an optimal combination of nanoparticle size, material and position for fixed laser parameters and the density profile of the gas target.

5.1 Gas target for ALFA experiment

The first set of simulations was carried out primarily to determine the impact of nanoparticle parameters on the accelerated beam. The reason is that the gas target for the ALFA experiment is only about 1 mm long, thus, these simulations are significantly less computationally expensive compared to the second set of simulations performed for the ELBA experiment with 20 mm long gas target. However, the process of electron injection facilitated by the nanoparticle is discussed as well.

In the end of this section a short discussion concerning the decision whether the nanoparticle injection scheme would be suitable for the ALFA experiment is given. The experiment is performed using multi-TW, 1 kHz laser system L1-Allegra and has already shown generation of collimated and quasi-monoenergetic electron beams with energy up to 50 MeV [56]. These results hold a promise towards developing high brilliance X-ray sources for medical imaging or novel devices for brain cancer treatment. We are interested in finding out, whether we can further improve these already impressive results.

5.1.1 Simulation parameters

As already mentioned, the laser used in this experiment was laser L1-Allegra. Thus, the laser central wavelength is $\lambda_L = 850$ nm, the focal spot is defined by $w_0 = 3$ μm and the pulse duration is $t_{FWHM} = 15$ fs (considering Gaussian profile

in time and space). The pulse energy is 40 mJ, which gives us the intensity of $I = 9 \times 10^{18}$ W/cm^2, and normalized vector potential $a_0 = 2.2$. Note, that pulse energy used for simulations is higher than in the experiment [56]. We made this decision to obtain higher intensity and a_0, based on the nominal pulse energy for laser L1-Allegra, which is 100 mJ. The laser is linearly polarized.

The size of the computational domain is 55×27.5 μm, the same as in the quasi-cylindrical simulation from the previous chapter. The cell size is 10.6×42.5 nm, hence, there are 5120 cells in the longitudinal direction and 640 cells in the transversal direction. The simulation time is set to $t_{sim} = 2266$ fs $= 800$ T_0 (T_0 is the laser period). Using the moving window algorithm, this corresponds to the total simulated length of 680 μm. The simulation timestep is set according to the CFL condition with $C = 0.95$.

The gas target, composed of nitrogen molecules, was also chosen according to the ALFA experiment, and its profile is depicted in fig. 5.1. The laser is focused in the gas target plateau at $z = 250$ μm. Only a part of this 1 mm long gas target was chosen for the simulation to reduce the computational cost. Also, for $z > 600$ μm the density of the gas target is set to zero to better distinguish accelerated electrons from the background. By running additional simulations, it was verified that these adjustments do not affect the results.
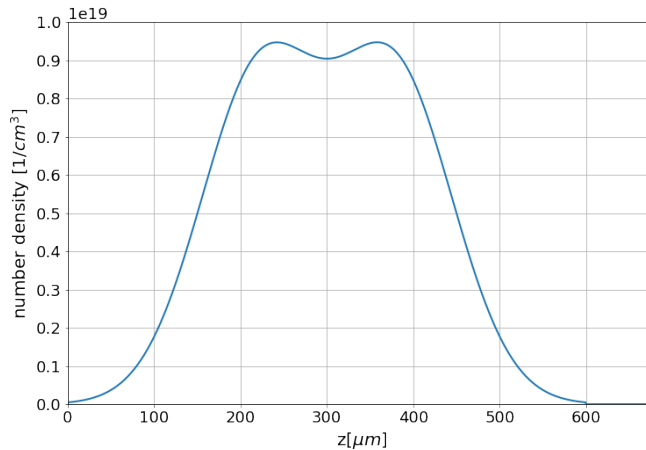
Figure 5.1: The dependency of the gas target density on longitudinal coordinate z. In the transversal direction a constant density profile is assumed.

The nanoparticle is defined as a sphere of diameter $d = 85$ nm with the center at $[z, 0]$. The nanoparticle is resolved using 8 cells (4 in the longitudinal direction, 2 in the transversal direction), whereas each oh these cells contains 1600 macro-particles. Note that one cell of nitrogen consists only of 16 macro-particles. In total, the simulation domain contains approximately 5.2×10^7 macro-particles. The whole simulation requires approximately 70 000 timesteps. Note, the process of ionization of the nitrogen as well as the nanoparticle is included in the simulation.

Performed simulations can be further divided in two sets. The first one is focused on parameters influencing the shape and amplitude of the plasma wave in the moment of electron injection, i.e. the plasma density and nanoparticle position. Note, the latter is connected to the laser waist, hence the intensity, at the moment when electron injection takes place. Since the Rayleigh range of the laser is only about 37 μm, the intensity of the laser significantly differs throughout the simulation even if we consider self-focusing of the laser pulse.

Therefore, two different gas target densities ($n = 9 \times 10^{18}$ cm^{-3} and $n = 1.6 \times 10^{19}$) and three different nanoparticle positions (z = 170 μm, z = 210 μm and z = 250 μm) were chosen to study the conditions during the electron injection and their influence on the accelerated electron beam. Gas target densities were chosen based on previous simulations. The first value $n = 9 \times 10^{18}$ cm^{-3} is the highest particle density at which the self-injection does not occur at all, while the higher value ($n = 1.6 \times 10^{19}$ cm^{-3}) corresponds to a particle density at which the energy spectrum of the electron beam, obtained from simulation with nanoparticle located at z = 210 μm, has a decent energy spread. Note, because of the laser parameters, a high density gas target was originally intended for this experiment (in ALFA $n = 5.7 \times 10^{19}$ cm^{-3} was used). Therefore, we want to use as high gas target density as possible, while preserving one of the main advantages of the nanoparticle injection scheme, which is low energy spread. Nanoparticle positions were simply chosen in the first half of the gas target so that the acceleration length is limited as little as possible.

The second set of simulations is focused on parameters of the nanoparticle, namely its size and material. For this purpose two different materials, already used in experiments ([8], [9]) were chosen - aluminium and copper. Moreover, three nanoparticle sizes were tested $d = 68$ nm, $d = 85$ nm and $d = 102$ nm. Note, for nanoparticle diameters $d = 68$ nm and $d = 102$ nm the simulation resolution had to be adjusted to model the nanoparticle. The new cell size was set to 8,5 $\times$ 34 nm, hence, the number of cells over the simulation domain has changed to 6400 in longitudinal and 800 in transversal directions and the required number of timesteps has risen to approximately 88 0000.

To sum up, parameters of all simulations, whose results will be presented in this section, are listed in table 5.1. In total 11 simulations were carried out. However, the results generally follow the same trend, hence, these results are not presented due to the limited space.

| Simulation number	1	2	3	4	5	6	7
nanoparticle size d[nm]	85	85	85	85	85	68	102
nanoparticle position z[μm]	210	170	250	210	210	210	210
nanoparticle material	Al	Al	Al	Al	Cu	Al	Al
gas target density n_e[10^{19} cm^{-3}]	1.6	1.6	1.6	0.9	1.6	1.6	1.6

Table 5.1: Table summarizing the parameters of performed simulations. Note, four more simulations were carried out (for 85 nm Al nanoparticles located at $z = 170$ μm and $z = 250$ μm with $n = 0.9 \times 10^{19}$ cm^{-3} and for Cu nanoparticles located at $z = 210$ μm with $d = 68$ nm and $d = 102$ nm and $n = 1.6 \times 10^{19}$). These results are not presented due to limited space.

5.1.2   Simulation results

In this section, the influence of nanoparticle parameters on the electron injection will be discussed. However, we shall start with a brief description of the whole acceleration process in this gas target, with emphasis on the injection process itself. For this purpose, the simulation with 85 nm aluminium nanoparticle located at $z = 210 \mu$m and gas target density $n = 1.6 \times 10^{19}$ cm^{-3} was chosen. Simulation with these parameters will also be used as a reference for future comparison.

The course of acceleration process (evolution of electric fields and the electron density) is illustrated in figure 5.2. The laser propagates from left to right, expelling electrons from its path and creating a linear plasma wave (case (a)). The plasma wave hereafter reaches highly nonlinear regime, this phenomenon is accompanied by creation of a positively charged cavity, also called a bubble (case (b)). At this point, one can also spot the ionized nanoparticle inside the bubble.

Moving on to case (c), we can already see the injected electrons represented by orange (gas electrons) and yellow (nanoparticle electrons) dots. For the sake of legibility, only a fraction of electron (macro-particles) with energy higher than 3 MeV is displayed. Note that the majority of nanoparticle electrons is injected into the first bubble, while the gas electrons mostly occupy the second one. As the laser propagates, it loses its energy mostly due to absorption in plasma and excitation of the plasma wave, moreover it is moving farther from the focal spot, hence, its intensity decreases. Consequently, the plasma wave weakens and its profile changes to weakly nonlinear (case (d)).
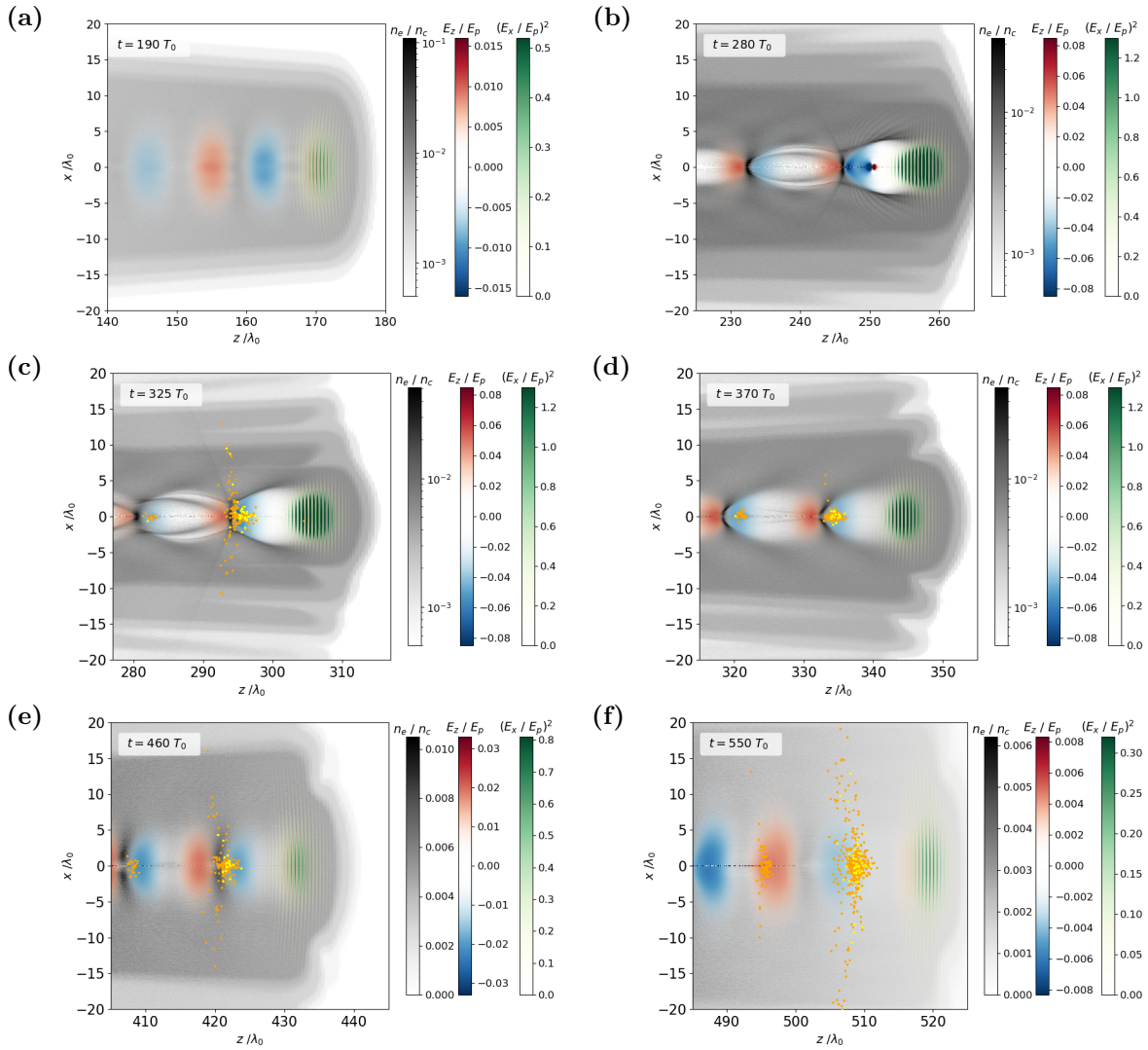

Figure 5.2: Electric fields (laser field and wakefield) and the electron density at different times (a) t = 190 T_0, (b) t = 280 T_0, (c) t = 325 T_0, (d) t = 370 T_0, (e) t = 460 T_0, (f) t = 550 T_0. Orange and yellow dots represent the electrons created by ionization from nitrogen molecules and aluminium nanoparticle, respectively. The color scales are saturated and in cases (a)-(d) the electron density is displayed in logarithmic scale.

In cases (e) and (f) we observe a further weakening of the driving laser pulse as well as a rapid decline of the electron density and consequently, a gradual dissipation of the plasma wave. In fig. 5.3(f) the electric field of the plasma wave is already too weak and is no longer able to accelerate injected electrons, thus, the acceleration length in this case is only about 200 μm. Note, for the case of the gas target density $n = 0.9\times10^{19}$ cm^{-3}, the evolution of electric fields and electron density distribution is very similar.

The injection process is illustrated by fig. 5.3, the first plot (a) captures the immediate moment after the interaction of the driving laser pulse and the nanoparticle. Ionization of the nanoparticle is illustrated by plotting tracked electrons (yellow dots) created by this process. At this point one can also notice a fraction of the plasma electrons (orange dots) with energy higher than 0.5 MeV. These electrons are currently forming edges of the bubble or are trapped in the electric field of the laser. Although case (b) displays electrons with energy higher than 0.5 MeV as well, at this moment, electrons with this energy are present in the whole plasma region. Hence, we observe plasma electrons being attracted by very strong electric field of the nanoparticle, (see fig. 5.4 to compare the electric field of the plasma wave with the electric field created by the ionization of the nanoparticle).

These electrons are injected into the accelerating field of the plasma wave, as shows case (c), which displays only electrons with energy over 2.5 MeV. It is clear that vast majority of the nanoparticle electrons was injected into the first period of the plasma wave, whereas the plasma electrons are present in both periods. One can also notice a significant amount of electrons forming a "bowtie" structure outside the acceleration field. Finally, in fig. 5.3(d) we can observe injected electrons in both plasma wave periods already without displaying the tracked macro-particles.
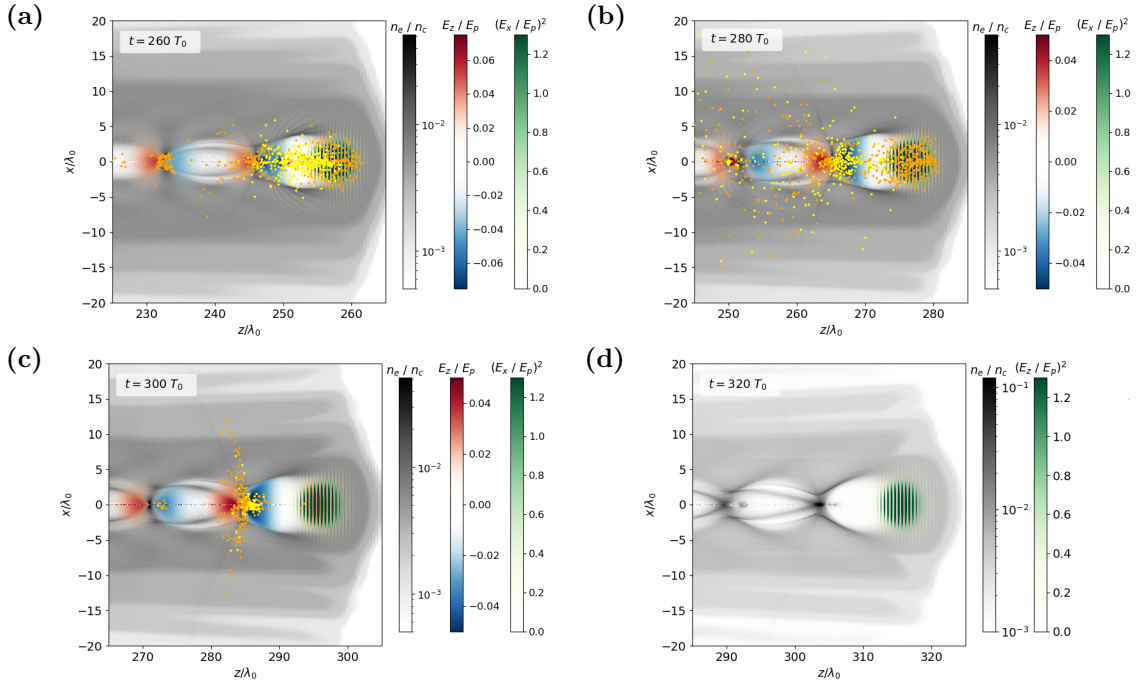

Figure 5.3: Illustration of the electron injection process, figures are plotted at (a) t = 260 T$_0$, (b) t = 280 T$_0$, (c) t = 300 T$_0$ and (d) t = 320 T$_0$. Orange and yellow dots represent electrons created by ionization from nitrogen and aluminium nanoparticle, respectively. Only a fraction of tracked particles is displayed for the sake of clarity.
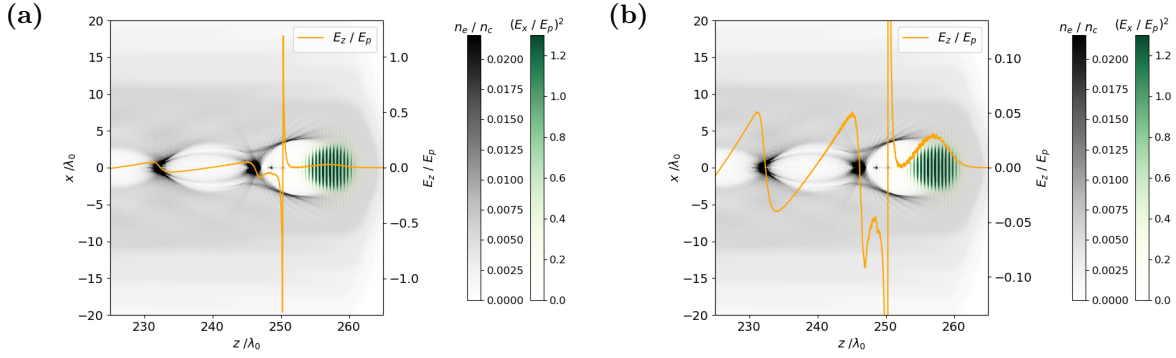
Figure 5.4: Illustration of the strength of the nanoparticle electric field compared to the electric field of the plasma wave. (a) At $z/\lambda_0 = 250$ the electric field of ionized nanoparticle is distinctive. This field is more than two orders of magnitude stronger than electric field created by the ionization of gas. (b) Closer look at the electric field of the plasma wave. For this purpose the maximum displayed value of the electric field was adjusted.

Electron injection

At this point, we will discuss the influence of various nanoparticle parameters on the electron injection, starting with the electron density and nanoparticle position in the gas target. These mostly influence the shape and amplitude of the plasma wave at the moment of the electron injection. Four different situations are depicted in fig. 5.5, showing plasma wave profiles at the moment of the nanoparticle ionization, hence, just before the electron injection.
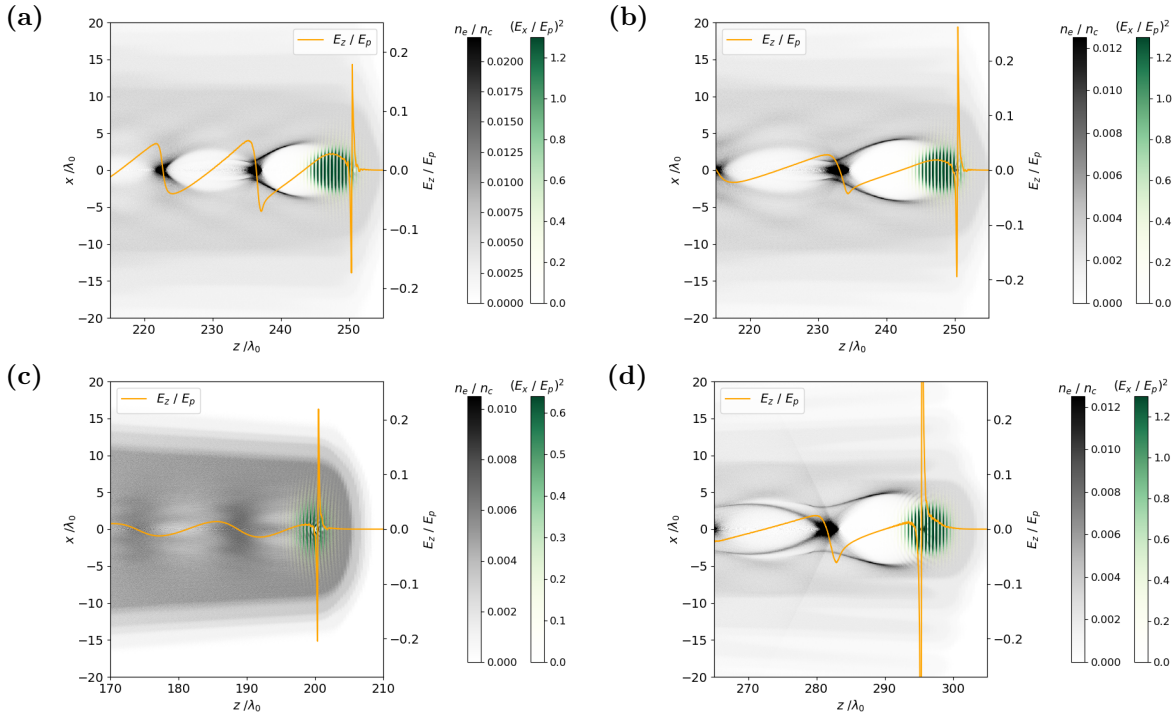

Figure 5.5: Plasma wave profile and amplitude before the electron injection for different gas target densities and nanoparticle positions; (a) $n = 1.6 \times 10^{19}$ cm^{-3}, $z = 210$ μm, (b) $n = 0.9 \times 10^{19}$ cm^{-3}, $z = 210$ μm, (c) $n = 1.6 \times 10^{19}$ cm^{-3}, $z = 170$ μm, (d) $n = 1.6 \times 10^{19}$ cm^{-3}, $z = 250$ μm.

The first two figures display the situation with nanoparticle at the same position but with different gas target density (a) $n = 1.6 \times 10^{19}$ cm^{-3} and (b) $n = 0.9 \times 10^{19}$ cm^{-3}. Consequently, in case (a) one can observe a plasma wave with shorter period and higher amplitude (electric field). Therefore, in case (a) one can expect more plasma electrons to be injected (because of the higher electron density) and accelerated to higher energies (because of the stronger accelerating field).

Secondly, we will compare figures with fixed gas target density and nanoparticles located at different positions ((a) $z = 210$ μm, (c) $z = 170$ μm and (d) $z = 250$ μm). Figure 5.5(c) shows quite weak, linear plasma wave, the reason is that the laser beam is still far from its focal plane, thus, its intensity is low. This will probably cause a low number of injected electrons and low beam charge. However, these electrons should gain the highest energies from all performed simulations.

The last situation, which will be described is depicted in fig.5.5(d). Despite the same gas target density as in case (a) was used, we observe a lower electron density at the moment of the nanoparticle ionization and subsequent electron injection. This can be caused, for example, by weakening of the laser pulse due to the ionization of the nitrogen gas. Therefore, one can again expect a lower charge of the accelerated electron beam. Note, in this case, it is not possible to compare the strength of the nanoparticle field, since the figures are not plotted at the exact same moment of the ionization and the strength of the nanoparticle electric field varies very quickly.

Moving to another set of simulations, we will now investigate how the electron injection is affected by different nanoparticle size and material. Figure 5.6 displays the difference in the ionization of the aluminium (a) and copper (b) nanoparticle. An atom of copper has more than twice the number of electrons than the aluminium atom. Moreover, the copper electrons are located in higher electron shells, hence, their ionization is easier. Therefore, in case of the aluminium nanoparticle a smaller amount of electrons is created, whereas the majority of them is trapped in the first bubble, as was already described. In case of the copper nanoparticle. However, a significant amount of nanoparticle electrons will be injected also into the second plasma period and we can not rule out that the injection will continue in the third or the fourth plasma wave period as well.
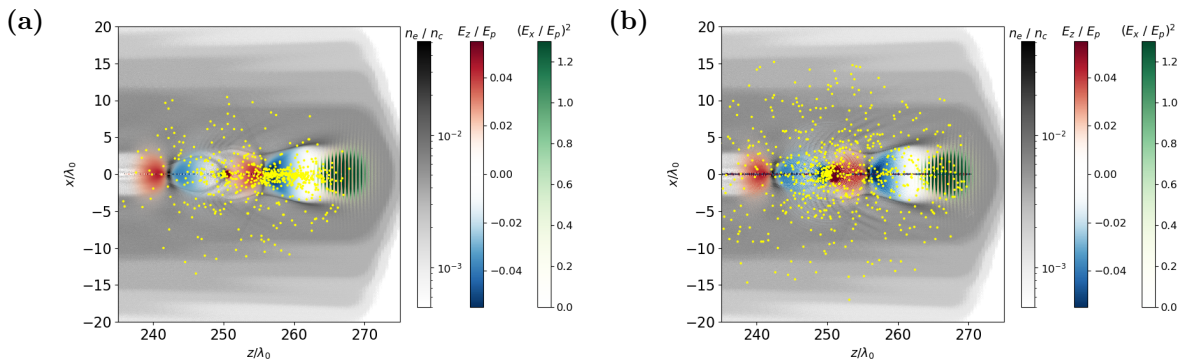
Figure 5.6: Comparison of the ionization of (a) aluminium and (b) copper nanoparticle. Significantly more electrons are created by the ionization of copper nanoparticle. One can also notice a strong noise introduced into the axis region of the simulation domain in case (b).

Moreover, the ionization of the copper nanoparticle creates a considerably stronger electric field than the aluminium one (see fig. 5.7). According to the theory described in section 1.4, this should cause injection of greater amount of electrons, hence, higher beam charge. This will be discussed in bigger detail in the following part of this section, which focuses on the parameters of the accelerated beam.

(a)   **(b)**
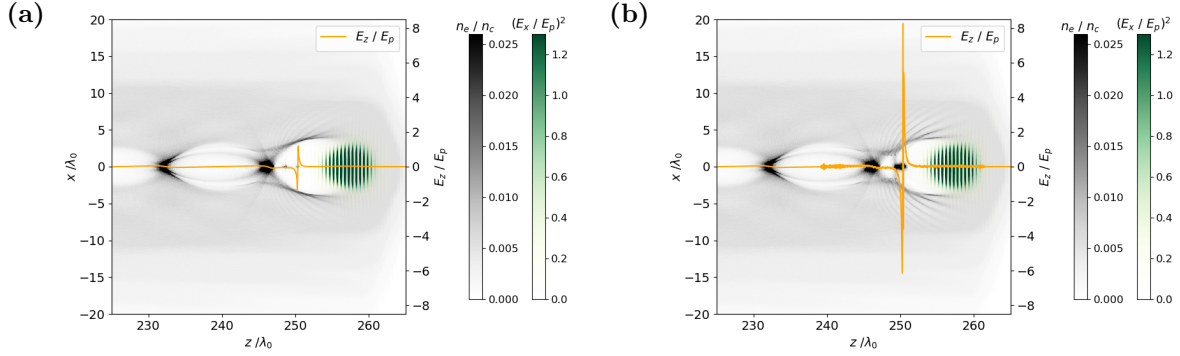
Figure 5.7: Comparison of the strength of the electric field created by ionization of (a) aluminium and (b) copper nanoparticle. The field in case (b) is considerably stronger. Note, the copper nanoparticle also causes more distinctive modulation of the plasma density around and in the bubble region. However, this is only temporary and without significant influence on the acceleration process.

A similar dependence can be observed for different nanoparticle sizes. From bigger nanoparticle a higher amount of electrons is created, thus, we should obtain higher beam charge. However, the strength of the electric field does not differ so immensely, only about 10 %. Therefore, we do not expect substantial electron injection in the third plasma wave period. Counter intuitively, slightly stronger electric field was generated by a smaller nanoparticle. At this time, we do not have a good explanation for this phenomenon.
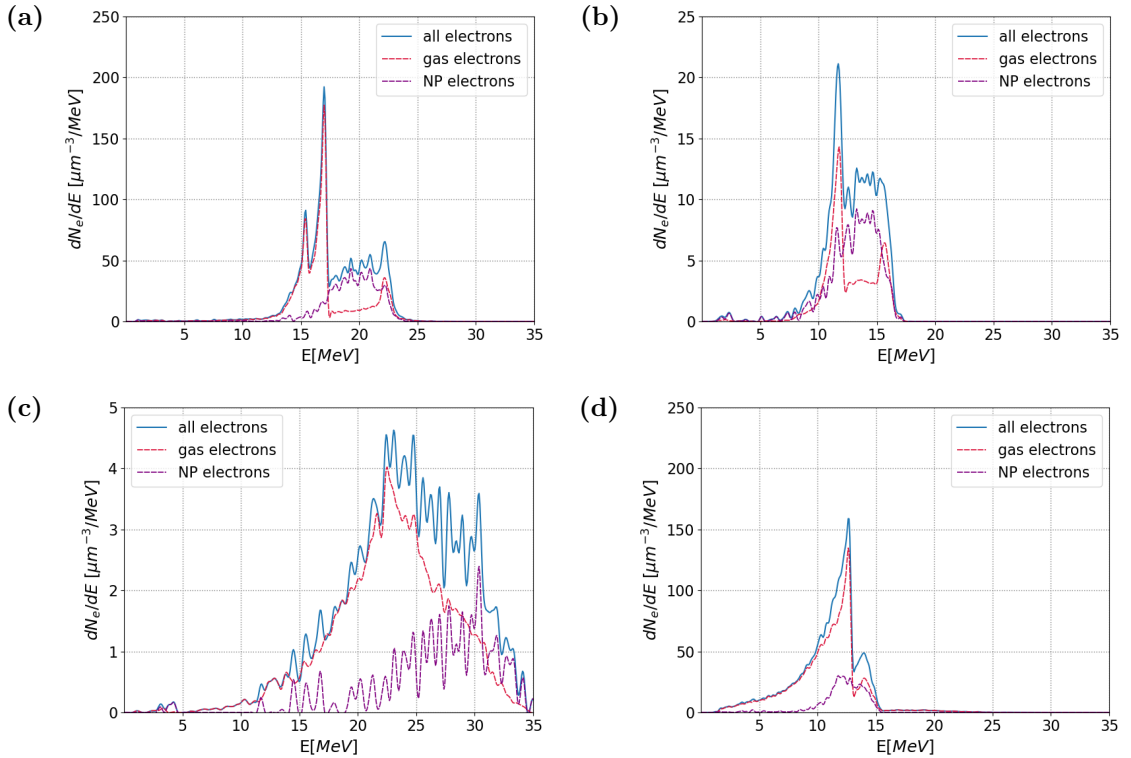
Electron beam

This part of chapter 5 is dedicated to the parameters of the accelerated electron beam. In the first place, the energy spectra will be discussed. For the sake of legibility, results are divided in two figures 5.8 and 5.9. The first one contains energy spectra for different nanoparticle positions and gas target densities, while the second one displays the same quantity for different nanoparticle sizes and materials. Every plot shows the energy spectrum of all accelerated electrons and also the respective contributions of electrons from plasma and from ionized nanoparticle. Note, these plots confirm most of our deductions from previous section.

Figures 5.8(a) and (b) capture electron energy spectra for different gas target densities. Due to stronger accelerating field the maximum achieved electron energy in case (a) $n = 1.6 \times 10^{19}$ cm^{-3} is about 5 MeV (22 %) higher than in case (b) $n = 0.9 \times 10^{19}$ cm^{-3}. Moreover, the amount of electrons injected in case (b) is approximately ten times lower, which is caused by both - lower gas target density as well as the weaker acceleration field. Similar phenomenon can be observed comparing cases depicting different nanoparticle positions (a) $z = 210$ μm,(c) $z = 170$ μm and (d) $z = 250$ μm. Moreover, from these plots, the dependency of maximum achieved energy on the acceleration length is apparent.

One can notice that the figure 5.8(c) significantly differs from the other cases in terms of energy spread and the amount of injected electrons. The reason for the latter one was already described in previous section. The wide energy spread arises probably due to self injection occurring in the plateau of the gas target, which is more distinctive in this case, because of the low amount of injected electrons by the ionization of the nanoparticle.

Another noteworthy fact is, that in both figures 5.8 and 5.9, the majority of nanoparticle electrons are accelerated to higher energies than the plasma electrons. In previous section we have found out that the nanoparticle electrons are mostly injected into the first plasma wave period. This is consistent with the fact, that the amplitude of the first plasma wave period is higher, which is also apparent from plots from the previous section.

Furthermore, comparing simulations for the gas target density $n = 1.6 \times 10^{19}$ cm^{-3} with nanoparticles (fig. 5.8 cases (a) and (d)) and the simulation without nanoparticle from the previous chapter (fig. 4.1), one can notice a significant growth in the amount of injected electrons. Thus, using nanoparticles it is possible to significantly increase the electron beam charge without changing any other parameters of the experiment. Note, that due to different scales on the y-axis, it may seem that maximum energies dropped if the nanoparticles were used. However, this is not the case and the maximum energies are approximately the same for all the simulations with $n = 1.6 \times 10^{19}$ cm^{-3}, except for the simulations with nanoparticles located at z = 170 μm. In this case, a low amount of electrons reached higher maximum energy due to the longer acceleration length.
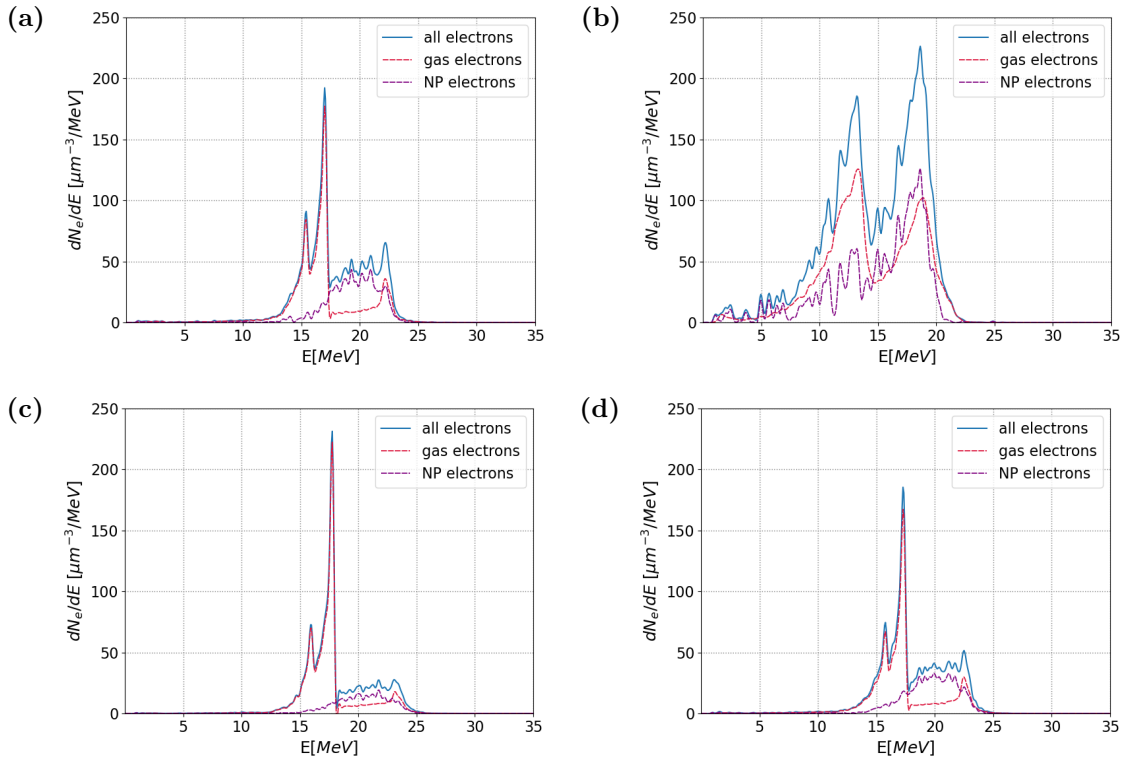

Figure 5.8: Energy spectra of accelerated electron beams obtained with different gas target densities and nanoparticle positions; (a) $n = 1,6 \times 10^{19}$ cm^{-3}, $z = 210$ μm, (b) $n = 0,9 \times 10^{19}$ cm^{-3}, $z = 210$ μm, (c) $n = 1,6 \times 10^{19}$ cm^{-3}, $z = 170$ μm, (d) $n = 1,6 \times 10^{19}$ cm^{-3}, $z = 250$ μm.

In terms of energy spread, a slight improvement from 15 MeV (fig. 4.1(b)) to approximately 10 MeV (fig. 5.8(a) and 5.8(d)) was achieved using the nanoparticles. This corresponds to a drop from approx. 35% to a little over 25% energy spread.

The second set of plots (fig. 5.9) depicts the electron energy spectra dependent on the nanoparticle size and material. If the copper nanoparticle is used (case (b)), one can observe a few times higher amount of injected and accelerated electrons, as was expected (and predicted by theory). Even though a slightly lower maximum energy was achieved, there is more electrons with energies between 15 and 20 MeV. One can also notice a bigger amount of injected electrons created by the ionization of the nanoparticle compared to simulations with aluminium nanoparticle.

As we expected based on results from the previous section, different nanoparticle size causes only minor changes to the electron spectrum. In cases (a), (c) and (d) one can notice a distinctive peak around approximately 17 MeV, which consists mainly of plasma electrons. Because the smaller nanoparticle (case (c) $d = 68$ nm) creates slightly stronger electric field more plasma electrons are injected. Whereas a smaller number of electrons is created by the ionization of the nanoparticle, thus, less of them is injected. This makes the mentioned peak even more distinctive.

Figure 5.9: Energy spectra of accelerated electron beams obtained with different nanoparticle materials and sizes; (a) Al, $d_{np} = 85$nm, (b) Cu, $d_{np} = 85$ nm, (c) Al, $d_{np} = 68$ nm, (d) Al, $d_{np} = 102$ nm.

To obtain more information about the distribution of the energy in the electron beam another set of plots, depicting longitudinal electron phase space, is presented (fig. 5.10). From this figure, it is apparent that electrons were injected in the first three plasma periods, creating three separate electron bunches. However, they are only few μm apart, which is distance too short to be detectable in any experiment. The only plot picturing solely two beams is 5.11(b) which corresponds to the simulation with lower gas target density ($n = 0.9 \times 10^{19}$ cm^{-3}).
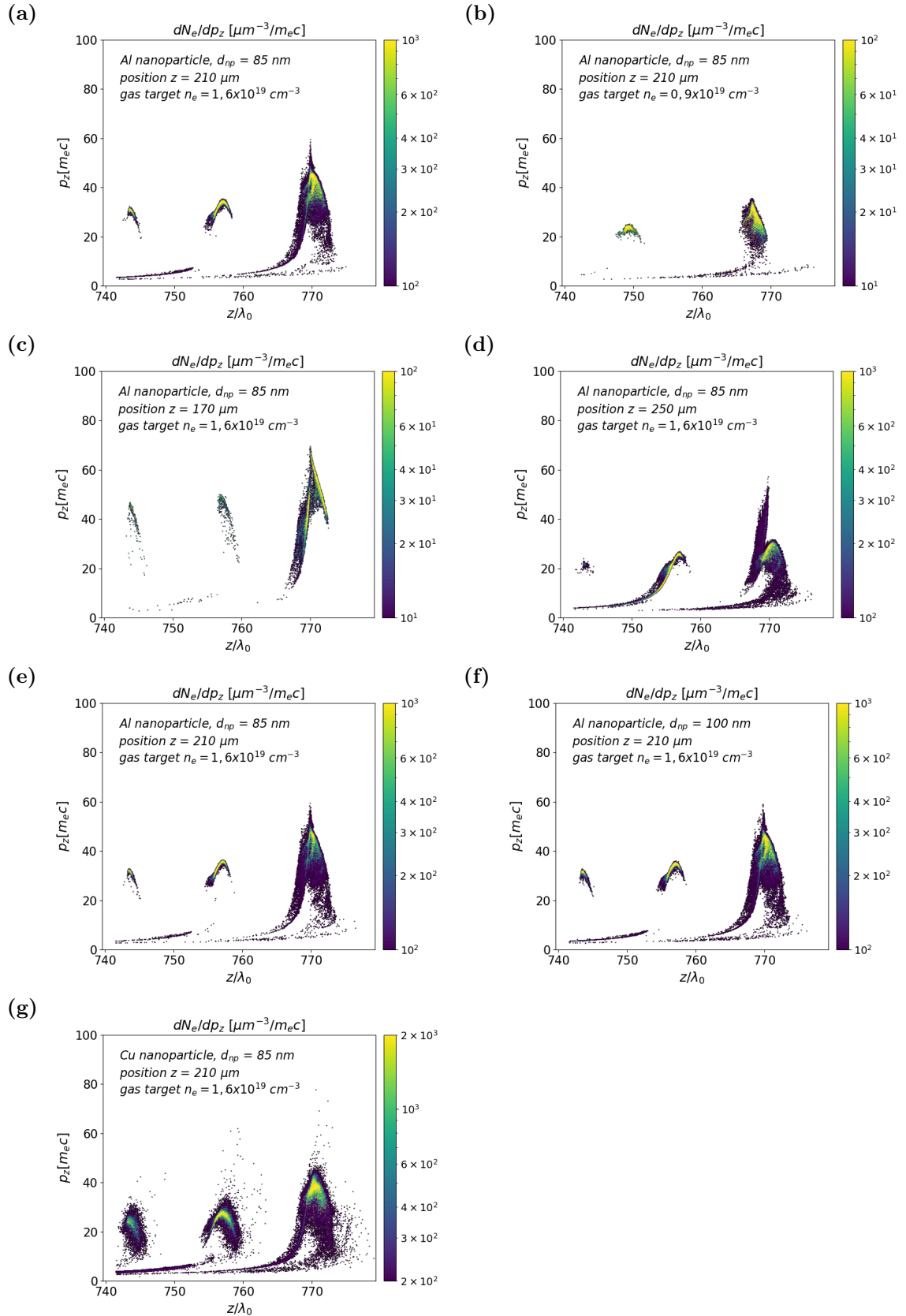
Figure 5.10: The longitudinal phase space of accelerated electron beams obtained with various simulation parameters, which are noted in the respective plots. The color scales are logarithmic and saturated.

Therefore, in this case the period of the plasma wave is longer. Thus, it is possible there is also a third beam but the simulation domain is too small to capture it. Note, in the other cases it seems only a part of the third beam is present in the plots. Another feature we can observe in cases (a), (e) and (f), displaying the phase spaces from simulations with different nanoparticle sizes, is that the distinctive peak in the electron spectra is indeed formed in the second plasma wave period. Moreover, one can notice also a smaller "secondary" peak present in the energy spectrum, which is most probably composed of electrons accelerated by the third plasma wave period. Since, as we mentioned, this beam is probably not completely captured in our simulations, it is reasonable to assume that this peak is in reality somewhat higher, than shows for example fig. 5.9(a).

Furthermore, in case (d) one can see a small amount of electrons reaching energies over 25 MeV (1 MeV corresponds to approximately 2 $m_e c$, which is a normalized unit of momentum in Smilei, see Appendix A). These electrons are not properly visible in the electron spectrum plot in fig. 5.8(d). Finally, taking a look at case (g), depicting the phase space from simulation with copper nanoparticle, one can notice that the second and third beam contain a considerably larger number of electrons than in any other simulation. This is also in agreement with our deduction from the previous section.

Finally, one more set of plots (fig. 5.11), related to the transversal profile of the electron beam, is presented. As a consequence of the linear laser polarization, all of those profiles are more or less elliptical, whereas the larger number of electrons is present in the accelerated beam (higher charge), the less is the ellipticity apparent. One can compare e.g. case (b) or (c) with the smallest beam charge, with case (g), where the biggest beam charge was achieved.

In most cases (a,d,e,f), the obtained beam charge is around 2.5 pC, these cases correspond to simulations with the same gas target density, nanoparticles with different sizes located at $z = 210$ μm and to simulation with nanoparticle at $z = 250$ μm. Based on our assumptions from the previous section, we did expect that these simulations will produce a similar beam charge. Moreover, in cases (b) and (c) one can notice the total beam charge is fairly lower (slightly over 0.5 pC) as a consequence of the lower gas target density (case (b)) and the unsuitable nanoparticle location (case (c)). Finally, the highest beam charge (7.6 pC) was achieved using copper nanoparticle instead of aluminium one, as a result of the stronger nanoparticle field as well as a greater number of electrons created by the nanoparticle ionization, which were subsequently injected into the accelerating field.

Note, the values of the total beam charge stated in the respective plots may not be entirely accurate for two reasons. On the one hand, our results from chapter 4 showed, that quasi-cylindrical simulations may overestimate the total number of injected electrons in comparison to full 3D simulations, which would results in higher beam charge than in reality. On the other hand, it was already mentioned that the simulation domain was not big enough to fully contain more than two plasma periods. Hence, in most cases the beam charge should be higher. This underestimation would be the most apparent in case (g), where the strongest electron injection is anticipated for reasons described in previous section. Nevertheless, in most cases, we can expect the total beam charge to be in order of few pC.

(a)

(b)

(c)

(d)

(e)

(f)

(g)
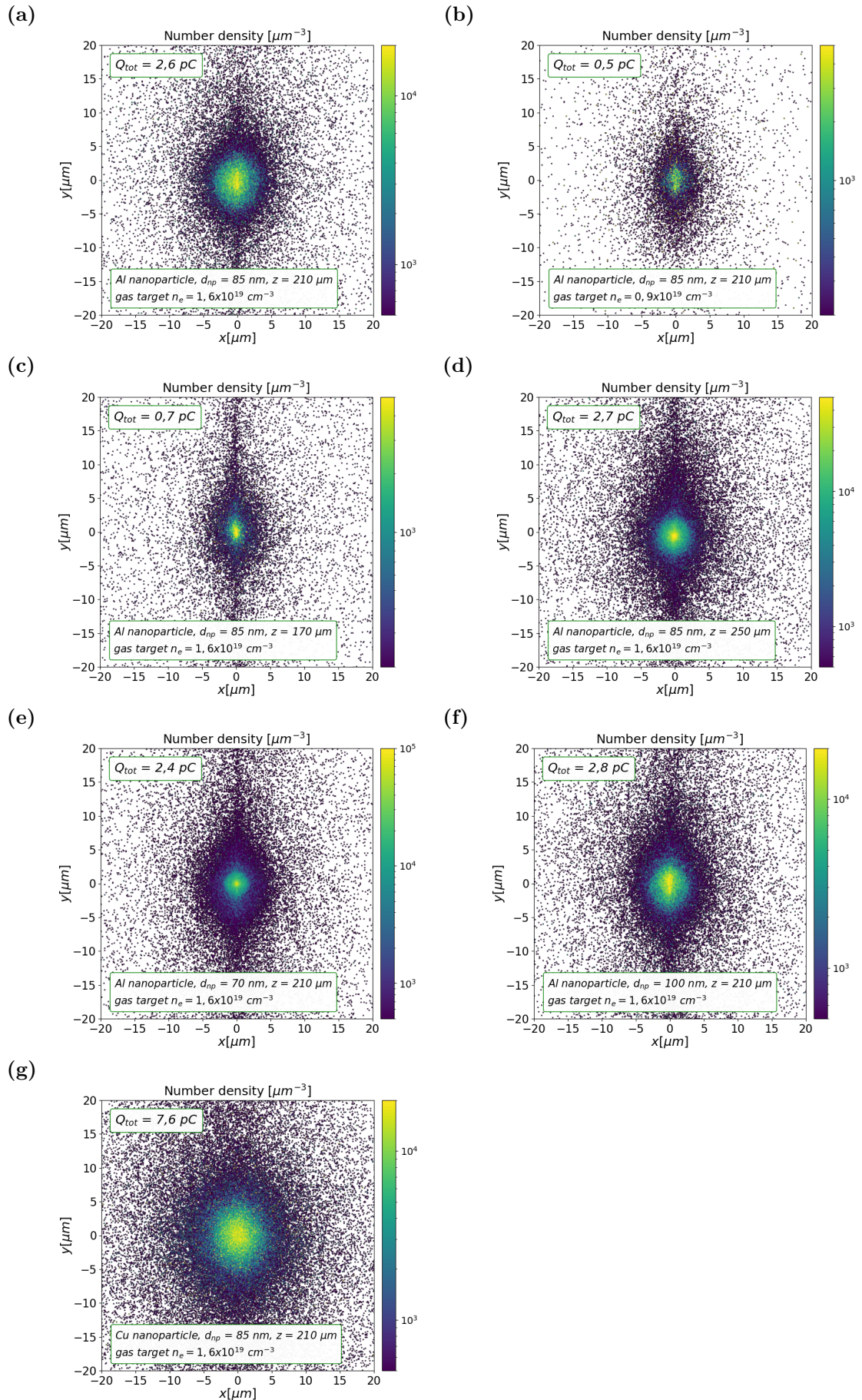
Figure 5.11: The transversal beam profiles obtained with various simulation parameters, which are noted in the respective plots. The color scales are logarithmic and saturated. The laser is linearly polarized along y-axis.

5.1.3   Summary

From the presented results is apparent that with this gas target density significant improvements in terms of the beam charge and energy spread can be achieved with the nanoparticle injection scheme. The most suitable nanoparticle position seems to be $z = 210$ μm, however, $z = 250$ μm is also a viable option. Unfortunately, with nanoparticle located at $z = 170$ μm there is only a minor improvement in the maximum energy, but the energy spread is worse than in case of the self injection. The fact that the results can vary distinctly, even if the nanoparticle is misplaced only by 40 μm, is a crucial problem for a possible utilization of this injection scheme in the ALFA experiment.

On the other hand, the fact that the nanoparticle size has rather minor influence on the parameters of the accelerated electron beam is a positive for future experiments. The reason is that the best way to create nanoparticles and deliver them to the gas target is currently the laser ablation, which is a technique that does not allow an exact control of the nanoparticle size. Moreover, a nanoparticle material offers control over the beam charge as well as the nanoparticle size, hence, we can tune the beam charge this way.

Concerning the suitability of the nanoparticle injection scheme for the ALFA experiment, we probably would not recommend it. Not only the maximum achieved energy is rather lower due to low gas target density and the energy spread is not improved in most cases, but this injection scheme brings further complexity to the experiment. Moreover, the greatest challenge lies in finding a way to deliver nanoparticles to the gas target with precision better than 100 μm (achieved in [9]). Otherwise it will not be possible to deliver stable electron beams because of the strong dependency of the beam parameters on the nanoparticle position.

5.2   Gas target for ELBA experiment

The second experiment, we are interested in, is called ELBA and it is focused mainly on achieving the highest energy (several GeV) and high-quality electron beams with the prospects of using them for fundamental science studies. To reach GeV energies, a long acceleration distance, hence, effective laser guiding, is necessary. Thus, the nanoparticle injection scheme, which allows the decoupling of the electron injection and laser pulse evolution, could be the right choice, for this experiment. Therefore, this section is more focused on finding the optimal parameters for a future experiment than on a parametric study of influence of the nanoparticle parameters.

5.2.1   Simulation parameters

The laser used for the ELBA experiment is laser L3-HAPLS, which is a Ti:sapphire system designed to generate 30 J pulses with duration $t_{FWHM} = 30$ fs, and central wavelength λ_L=800 nm. The laser system generates a square flat top beam in space. However, for the experiment the laser will be focused and have a Gaussian profile with focal spot $w_0 = 52$ μm. Since a certain amount of the laser energy can be lost during the guiding and focusing, we will assume the energy contained in the pulse is 20 J. These parameters yield intensity approximately 9.8 $\times 10^{18}$ Wcm^{-2} and normalized vector potential $a_0 = 2.1$.

The gas target profile, chosen according to the experiment, is depicted in fig. 5.12. It is approximately 20 mm long, formed by helium molecules, whereas its density is set to $n = 1.5 \times 10^{18}$. However, the ionization of the gas is not included in this simulation, we assume the helium is fully ionized, hence, the plasma density is set to $n_e = 3 \times 10^{17}$ cm^{-3}. This value was determined by preliminary analytic calculations to obtain dephasing and depletion length roughly the same as the gas target length. The laser focus is at $z = 7$ mm.
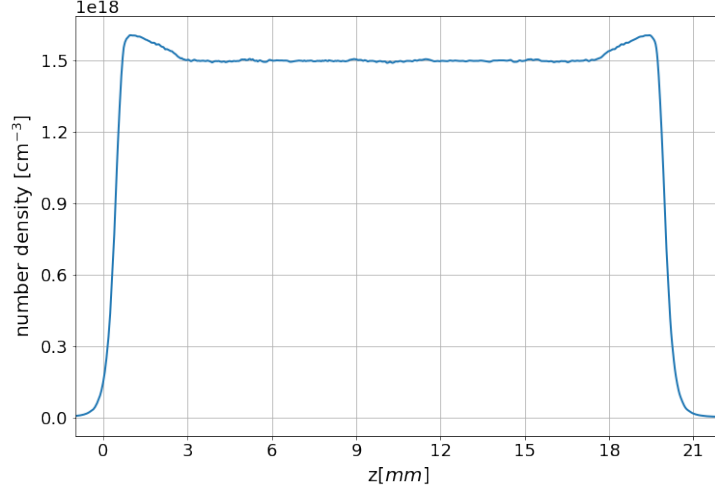
Figure 5.12: The dependency of the gas target density on longitudinal coordinate z. In the transversal direction a constant density profile is assumed.

Computational domain dimensions are 155×110 μm, to properly contain the laser pulse and prevent its reflection at the borders of the grid. Since running the whole simulation with the resolution necessary to resolve the injection facilitated by the nanoparticle would be very computationally expensive even using the cylindrical geometry, we decided to divide the simulation into two parts.

First, we simulated the whole gas target (20 mm) without the nanoparticle to establish the strength of the accelerating field. In this case, the used cell size was 40×160 nm, which makes 3840 cells in the longitudinal and 800 cells in the transversal direction. The total simulation time using the moving window is approximately 62 ps (24 000 T_0).

The purpose of the second simulation is to study the electron injection. Hence, the simulation resolution had to be enhanced to 10×40 nm and consequently, the number of cells increased to $13\,900 \times 3200$ cells. The nanoparticle is located at the beginning of the gas target ($z \approx 3$ mm). We are interested only in the electron injection, hence, the simulation starts 200 μm before the nanoparticle and ends after 400 μm. The plasma density is assumed constant over in this simulation. The simulation time is $t = 500$ T_0. In both cases, the simulation timestep is set according to the CFL condition (C = 0.95). The nanoparticle is defined in the same manner as in previous simulations as well as the number of macro-particles per cell. This yields approximately 4.9×10^7 macro-particles per cell for the first simulation and 7.1×10^8 macro-particles per cell for the simulation with the nanoparticle. Note, we omitted the ionization of the gas for this simulations, however, the ionization of the nanoparticle is taken into account.

For this gas target we eventually decided to run only two simulations to study the electron injection, one with aluminium and one with copper nanoparticle. This

decision was based on results presented in the previous section and on the fact that
the optimal gas target density is determined by the laser parameters.

Furthermore, we want to place the nanoparticle at the beginning of the gas target
to obtain the longest acceleration length possible. Because the Rayleigh range of this
laser is about 8 mm and the achieved precision of nanoparticle placement in previous
experiment [9] is 100 μm, there is no point in studying the influence of nanoparticle
position on the electron injection. Finally, the influence of the nanoparticle size on
the electron injection process is not as significant. Besides, this would be better to
inspect once we know how big nanoparticles we can create for the experiment.

Note, we also ran a simulation with a 10 J laser pulse ($a_0 = 1.56$), which cor-
responds to energy slightly lower than the current pulse energy generated by the
L3-HAPLS system. However, with this setup we did not detect any injected elec-
trons, even after increasing the plasma density. Hence, we deduced that the laser is
too weak to create sufficiently strong electric field of the plasma wave to facilitate
the electron injection (even if the nanoparticle is present). Better and more detailed
explanation would require further examination.

5.2.2   Simulation results

In this section, results from the last two simulations performed for this thesis will
be described. First, a plot depicting the moment of the aluminium nanoparticle
ionization (fig. 5.13) is presented. One can notice the contrast between the electric
field of the nanoparticle and the longitudinal electric field of the plasma wave is
similar to the situation from the previous section. Similar behaviour shows also the
simulations with the copper nanoparticle.

The plasma wave is in weakly nonlinear regime, to which corresponds also the
distribution of the electron density. In the second plasma wave period, we observe
a light disruption in the electron density, which is most probably caused by the
sharp edge of the plasma region (the laser propagates in vacuum for 50 λ_0 and then
hits the plasma with the constant profile). This disruption diminishes as the laser
propagates further.
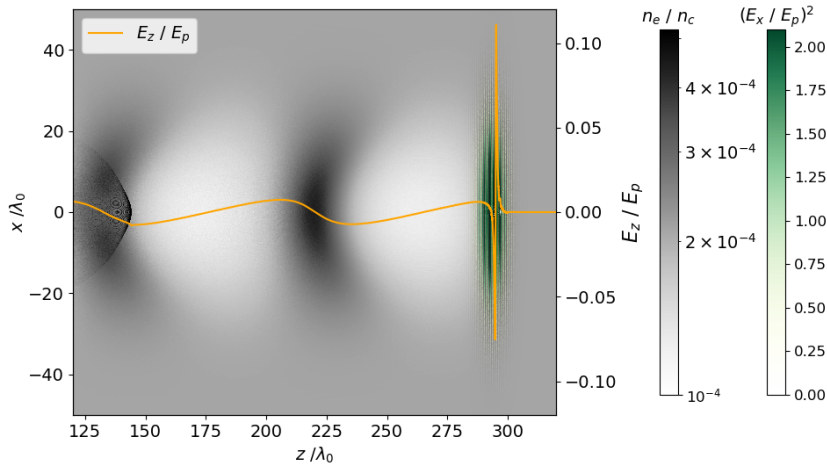
Figure 5.13: Electron density distribution (grey), the laser pulse (green) and the profile
of the longitudinal electric field at $x \approx 0$ (orange line).

The next figure (5.14) offers look at the electric fields created by the ionization of the aluminium and copper nanoparticle. From this picture is obvious that not only the electric field created by the copper nanoparticle is stronger, it is also more spread out. This will have an influence on the electron density distribution, which we already observed in the previous section.

However, in the case of the ALFA experiment the perturbation of the electron density is significantly stronger. Therefore, the impact of the nanoparticle electric field on the electron density distribution and the accelerations process is only minor. This fact is not true for the ELBA experiment and will be discussed in the next paragraphs.
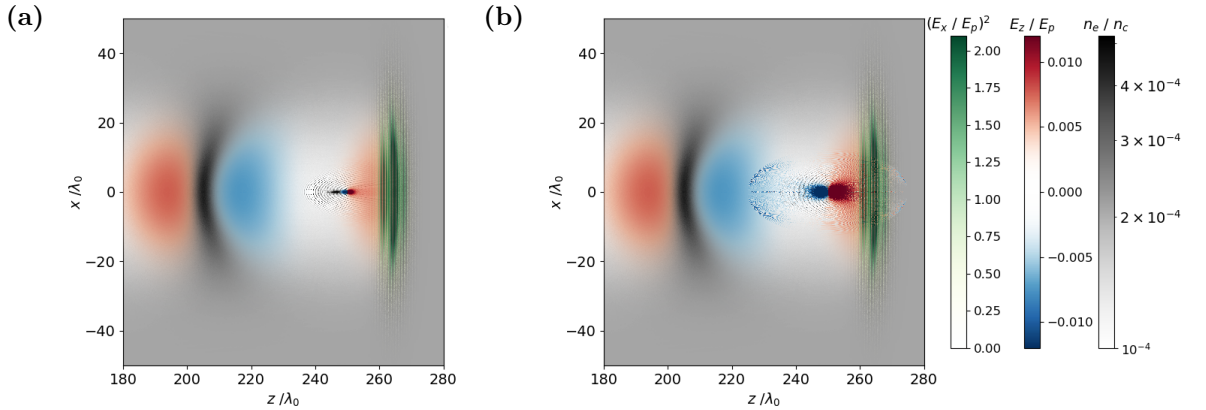

Figure 5.14: Comparison of the electric field created by the ionization of (a) aluminium and (b) copper nanoparticle. Significantly stronger and widespread electric field is created by the ionization of copper nanoparticle.

Figure 5.15 depicts the injected electrons symbolized by yellow (nanoparticle) and orange (plasma) dots for nanoparticles from different material. Results from the simulation with aluminium nanoparticle (case (a)) are in agreement with our previous conclusion, the majority of the electrons created by the nanoparticle ionization is injected into the first plasma wave period, while the plasma electrons are mostly present in the second period.

However, if the copper nanoparticle was used (case (b)) we observe several differences. First, one can notice the distribution of the electron density is distinctively disturbed by electric field of the ionized nanoparticle. Furthermore, even though in the first plasma wave period we observe a larger amount of nanoparticle electrons than in the previous case (as expected), it seem there is less electrons present in the second period. This is in contradiction with our expectations, stronger electric field created by the ionization of the copper nanoparticle should attract more plasma electrons. Moreover, electrons in plasma wave periods are not forming a narrow beam as one can see in case (a), which is probably caused by the electron density distortion.

Nevertheless, at the end of the second plasma wave period one can observe an instability at the axis of the simulation domain, created by the ionized nanoparticle. Therefore, it is possible that the results at this region are not accurate. It is currently not clear, whether this is caused solely by the strong electric field of the nanoparticle or whether the specific numerical treatment of the electromagnetic fields in the cylindrical geometry at the axis also played a role. Probably it is a combination of both, since we observe this instability also later in the simulation (see fig. 5.16).

Unfortunately, we were not able to find a way to completely eliminate this instability. Nonetheless, we plan to perform a full 3D simulation for further examination.
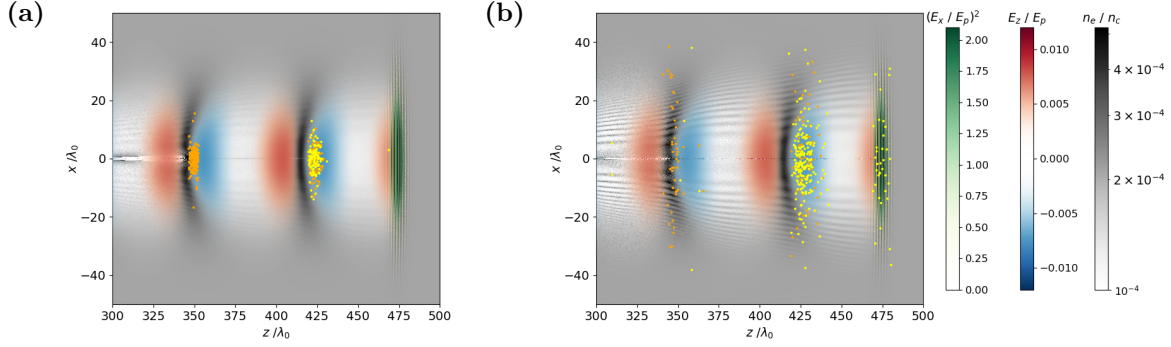
Figure 5.15: Illustration of the injected electrons using (a) aluminium and (b) copper nanoparticle. Yellow and orange dots represent electrons from the ionized nanoparticle and from plasma, respectively. Both figures are plotted at t = 500 T_0.

The last figure presented (5.16) depicts the further development of the electron density and injected electrons in case the copper nanoparticle was used. We can observe the distortions in electron density gradually diminishing and electrons in the first plasma wave period forming a narrower beam. Therefore, we assume that the electron beam divergence is caused by the electron density perturbation.
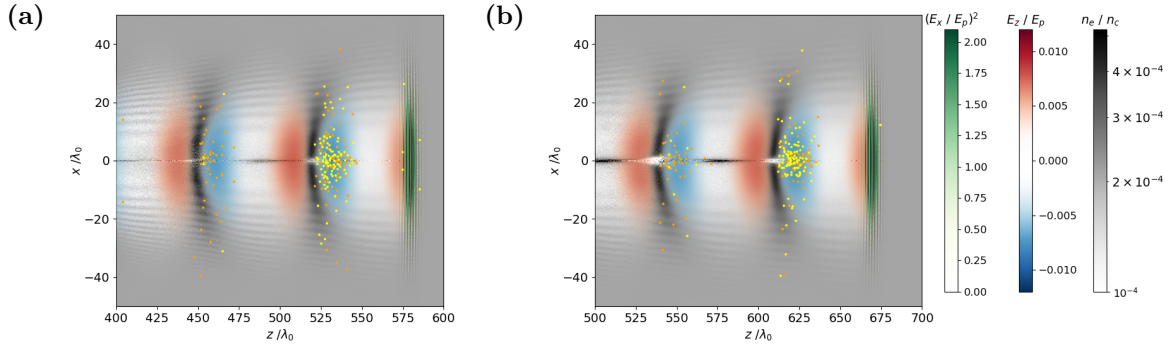
Figure 5.16: Illustration of the development of the injected electrons using the copper nanoparticle. Blue and green dots represent electrons from the ionized nanoparticle and from plasma, respectively. Figures are plotted at (a) t = 600 T_0 (b) t = 700 T_0.

5.2.3   Summary

Because the gas target for ELBA experiment was too long to simulate the whole acceleration process and do a parametric study, like in the case of the ALFA gas target, we decided to perform two different types of simulations. One with fine resolution to study only the electron injection and the second one to examine the evolution of the plasma wave thorough the gas target.

Furthermore, we wanted this simulation to be a baseline for a future experiment at ELI Beamlines. Hence, the majority of parameters (e.g. the gas target profile and density and nanoparticle size) has been already determined by the available equipment. Moreover, the nanoparticle should be placed at the beginning of the gas target, to obtain the longest acceleration length possible. Therefore, the only relevant nanoparticle parameter, whose influence on the electron injection seemed

worth to study, is the nanoparticle material. This decision was also supported by the results from the previous section.

The simulation performed to study the evolution of the plasma wave showed the amplitude of the accelerating field varied from 20 GV/m to 45 GV/m over the whole simulation. Whereas at about 17 mm, the electric field of the plasma wave started to weaken. By a rough estimate, the maximum energy of the accelerated electrons should be around 600 MeV. Therefore, to reach the electron energy over 1 GeV several adjustments need to be made. One possible solution is to design a longer gas target with lower density to get a longer acceleration length. However, to obtain a more suitable gas target profile, which could also be used for the experiment, requires running CFD simulations of supersonic gas jets, which create the gas target.

A second way to accelerate electrons to higher energies is to use laser with higher intensity. This can be achieved, while retaining the same laser energy, e.g. by focusing laser into a tighter spot. Unfortunately, this could result in higher divergence of the laser pulse and, more importantly, it would require extensive tests in the laboratory.

To sum up, the nanoparticle injection scheme is certainly suitable for the ELBA experiment. If we were to suggest a parameters of a nanoparticle gas target, using only currently available equipment, we would use the gas target from fig. 5.12, with density about $n = 1.25 \times 10^{18}$ cm^{-3}, to better match the pump depletion length. Based on results from this section, the nanoparticle material should be aluminium and the position of the nanoparticle would remain at $z \approx 3$ mm. Nevertheless, to design a nanoparticle gas target with potential to accelerate electrons to GeV energies, further adjustments need to be made. We plan to continue pursuing this goal in the future.

Conclusion

This master's thesis handles the novel electron injection scheme proposed for the laser wakefield acceleration. This injection scheme uses nanoparticles to achieve robust and localized electron injection, with a possibility to obtain high energy electron beams with very small energy spread. Furthermore, by the suitable choice of the nanoparticles parameters (such as diameter or density) or their position, one can to a certain extent control the parameters of the electron beam. The main purposes of this thesis were to examine an influence of the nanoparticle parameters on the injection process and accelerated electron beam, determine whether the nanoparticle injection scheme is suitable for experiments at ELI Beamlines and if so, propose a parameters of the gas target for such an experiment.

The first three chapters are devoted to a theoretical introduction. The first chapter covers the basic physics involved in the process of laser wakefield electron acceleration (LWFA). Then, a brief description of the PIC algorithm, which was used to investigate the nanoparticle influence on the acceleration process, as well as a short introduction of the PIC code Smilei, used for running simulations within this work, are provided in the second chapter. The third chapter is dedicated to advanced numerical techniques implemented in various PIC codes to reduce the computational cost of the simulation. The techniques chosen for performing simulations (azimuthal modes decomposition) is discussed in a detail.

In the fourth chapter, a comparison of a full 3D and quasi-3D (cylindrical) simulation is given. First, the computational demands of a full 3D simulation using the mesh refinement technique compared to a quasi-cylindrical simulation are discussed. Even though, the cylindrical simulation requires a finer resolution, it is still a less computationally expensive approach, especially if a big computational grid is required. The second part of this chapter is focused on the comparison of results obtained using the two above mentioned geometries. A good resemblance in the majority of aspects (electron density distribution, energy spectrum and profile of the accelerated electron beam) is achieved with both approaches. The only notable difference is in the number of accelerated electrons, which is overestimated by the quasi-3D simulation. This fact is taken into account in the next chapter while discussing results of our simulations.

The last chapter contains results from several PIC simulations, studying the influence of nanoparticle parameters on acceleration process. At first, we thoroughly examined the influence of different nanoparticle size, material and position on the energy spectrum, charge and profile of accelerated beam in a 1 mm long gas target used for the ALFA experiment. With majority of parameters combinations we obtained electron beams with mean energies from 13 to 17 MeV. The only exception was the simulation with nanoparticle located in the up-ramp region of the gas target. In this case, the mean energy of the electron beam is about 25 MeV, but the

energy spread is considerably wider than in other simulations.

We also verified that it is possible to significantly increase the charge of the accelerated electron beam, especially by using nanoparticles made from high density (and high Z) materials. Assuming the same gas target density $n = 1.6 \times 10^{19}$ cm^{-3}, the estimated electron beam charge without the nanoparticle is few hundreds fC. Whereas with the aluminium nanoparticle this value increased to approximately 2.5 pC and with copper nanoparticle to even 7.6 pC. The second value would mean also a considerable improvement compared to the results achieved in ALFA experiment, although at a cost of lower energy.

We also observed a strong dependence of the beam parameters on the nanoparticle positions in the gas target, which is caused by a different strength of the plasma wave electric field at these positions. Unfortunately, this fact makes the nanoparticle injection scheme rather unsuitable for the ALFA experiment, since we are currently not able to deliver nanoparticles with required precision.

The second part of the last chapter is focused mainly on the determining suitable parameters for the ELBA experiment generating electron beams with GeV energies at ELI Beamlines. Since long accelerating distances are required to obtain electrons with energies this high, a 20 mm long gas target was designed for this experiment. In this case, we do not need to deliver nanoparticles to the gas target as precisely so the nanoparticle injection scheme could be a great advantage for the ELBA experiment.

The density of the gas target $n = 1.25 \times 10^{18}$ cm^{-3} was chosen to obtain dephasing and depletion length roughly the same as the gas target length. Furthermore, we propose the usage of aluminium nanoparticles positioned at $z \approx 3$ mm. The size of the nanoparticles will be (to some extent) determined by the parameters of the laser used for the ablation, however, a smaller nanoparticles seem to be beneficial for lower energy spread.

In the future, we plan to finish the optimization of the parameters of the nanoparticle gas target and perform an experiment using our design. The ultimate goal of the experiment is generation of stable and high quality electron beams, which can be used for further research. Moreover, we would like to perform additional simulations to examine some of the observed phenomena, e.g. the electron density perturbation in the bubble structures created by the the ionization of the copper nanoparticle in the simulation of the ELBA gas target, or the cause of the instability at the axis of the simulation domain in the same simulaiton.

Bibliography

[1]   T. Tajima and J. M. Dawson, "Laser electron accelerator", *Physical Review Letters*, vol. 43, pp. 267–270, 1979.

[2]   F. Albert and A. G. R. Thomas, "Applications of laser wakefield accelerator-based light sources", *Plasma Physics and Controlled Fusion*, vol. 58, 2016.

[3]   W. P. Leemans, B. Nagler, A. J. Gonsalves, *et al.*, "Gev electron beams from a centimetre-scale accelerator", *Nature Physics*, vol. 2, pp. 696–699, 2006.

[4]   B. B. Pollock, C. E. Clayton, J. E. Ralph, *et al.*, "Demonstration of a narrow energy spread, 0.5 gev electron beam from a two-stage laser wakefield accelerator", *Physical Review Letters*, vol. 107, 2011.

[5]   J. P. Couperus, R. Pausch, A. Köhler, *et al.*, "Demonstration of a beam loaded nanocoulomb-class laser wakefield accelerator", *Nature Communications*, vol. 8, 2017.

[6]   V. Malka, "Laser plasma accelerators", *Physics of Plasmas*, vol. 19, pp. 055501-055501–11, 2012.

[7]   M. H. Cho, V. B. Pathak, H. T. Kim, and C. H.Nam, "Controlled electron injection facilitated by nanoparticles for laser wakefield acceleration", *Scientific Reports*, vol. 8, pp. 1–8, 2018.

[8]   C. Aniculaesei, V. B. Pathak, K. H. Oh, *et al.*, "Proof-of-principle experiment for nanoparticle-assisted laser wakefield electron acceleration", *Physical Review Applied*, vol. 12, pp. 41–51, 2019.

[9]   J. Xu, L. Bae, M. Ezzat, *et al.*, "Nanoparticle-insertion scheme to decouple electron injection from laser evolution in laser wakefield acceleration", *Scientific Reports*, vol. 12, 2022.

[10] J. Wenz and S. Karsch, "Physics of laser-wakefield accelerators (lwfa)", in *Proceedings of the 2019 CERN–Accelerator–School course on High Gradient Wakefield Accelerators*, Jul. 2019.

[11] B. Cros, "Laser-driven plasma wakefield: Propagation effects", in *Proceedings of the CAS-CERN Accelerator School: Plasma Wake Acceleration*, Nov. 2016, pp. 207–230.

[12] G. M. Grittani, "A study of gev electrons by laser-plasma acceleration for secondary radiation sources", M.S. thesis, Università di Pisa, 2013.

[13] F. Chen, *Introduction to Plasma Physics and Controlled Fusion.* Springer, 1984, ISBN: 978-3-319-22308-7.

[14] D. R. Nicholson, *Introduction to Plasma Theory.* Wiley, 1983, ISBN: 978-0471090458.

[15]   P. Gibbon, "Introduction to plasma physics", in *CAS-CERN Accelerator School: Plasma Wake Acceleration*, Nov. 2014.

[16]   P. Valenta, "Tight-focusing of short intense laser pulses in particle-in-cell simulations of laser-plasma interaction", M.S. thesis, Czech Technical University in Prague, 2017.

[17]   E. Esarey, C. B. Schroeder, and W. P. Leemans, "Physics of laser-driven plasma-based electron accelerators", *Reviews of Modern Physics*, vol. 81, pp. 1229–1285, 2009.

[18]   H. T. Kim, V. B. Pathak, C. I. Hojbota, *et al.*, "Multi-gev laser wakefield electron acceleration with pw lasers", *Applied Sciences*, vol. 11, 2021.

[19]   R.Bingham and R. Trines, "Introduction to plasma accelerators: The basics", in *Proceedings of the 2016 CERN–Accelerator–School course on High Gradient Wakefield Accelerators*, Nov. 2016.

[20]   P. Gibbon, "Introduction to plasma physics", in *Proceedings of the 2014 CAS-CERN Accelerator School: Plasma Wake Acceleration*, Nov. 2014.

[21]   J. M. Dawson, "Nonlinear electron oscillations in a cold plasma", *The Physical Review*, vol. 113, pp. 383–387, 1959.

[22]   A. Pukhov and J. Meyer-ter-Vehn, "Laser wake field acceleration: The highly non-linear broken-wave regime", *Applied physics B - Lasers and Optics*, vol. 74, pp. 355–361, 2002.

[23]   S. Lorenz, "Characterization of gas targets for laser plasma electron acceleration", M.S. thesis, Czech Technical University in Prague, 2019.

[24]   S. Bulanov, N. Naumova, F. Pegoraro, and J. Sakai, "Particle injection into the wave acceleration phase due to nonlinear wake wave breaking", *Physical Review E*, vol. 58, pp. 5257–5260, 1998.

[25]   M. van der Wiel, O. Luiten, G. Brussaard, *et al.*, "Laser wakefield acceleration: The injection issue. overview and latest results", *Philosophical Transactions of the Royal Society A*, vol. 364, pp. 679–687, 2006.

[26]   V. B. Pathak, H. T. Kim, J. Vieira, and a. N. C. L. Silva, "All optical dual stage laser wakefield acceleration driven by two-color laser pulses", *Scientific Reports*, vol. 8, 2018.

[27]   K. Schmid, A. Buck, C. M. S. Sears, *et al.*, "Density-transition based electron injector for laser driven wakefield accelerators", *Physical Review Special Topics - Accelerators and Beams*, vol. 13, 2010.

[28]   J. Faure, "Plasma injection schemes for laser–plasma accelerators", in *Proceedings of the 2014 CAS-CERN Accelerator School: Plasma Wake Acceleration*, Nov. 2014.

[29]   C. Rechatin, X. Davoine, A. Lifschitz, *et al.*, "Observation of beam loading in a laser-plasma accelerator", *Physical Review Letters*, vol. 103, 2009.

[30]   K. Virk, "A review on self focusing in laser plasma interaction", *Materials Today: Proceedings*, vol. 37, pp. 2786–2791, 2021.

[31]   J. P. Palastro, J. L. Shaw, P. Franke, D. Ramsey, T. T. Simpson, and D. H. Froula, "Dephasingless laser wakefield acceleration", *Physical Review Letters*, vol. 124, 2020.

[32] E. Esarey, B. A. Shadwick, C. B. Schroeder, and W. P. Leemans, "Nonlinear pump depletion and electron dephasing in laser wakefield", in *AIP ADVANCED ACCELERATOR CONCEPTS: Eleventh Advanced Accelerator Concepts Workshop*, Jun. 2004.

[33] J. P. Verboncoeur, "Particle simulation of plasmas: Review and advances", *Plasma Physics and Controlled Fusion*, vol. 47, no. 5A, A231, 2005.

[34] R. W. Hockney and J. W. Eastwood, *Computer simulation using particles.* Bristol: IOP Publishing Ltd, 1988, ISBN: 0-85274-392-0.

[35] H. Fehske, R. Schneider, and A. W. (Eds.), *Computational Many-Particle Physics.* , Berlin Heidelberg: Springer, 2008.

[36] L. Brieda, *Plasma Simulations by Example.* Boca Raton: CRC Press, 2019, ISBN: 978-1-138-34232-3.

[37] J. Derouillat, A. Beck, F. Pérez, *et al.*, "Smilei: A collaborative, open-source, multi-purpose particle-in-cell code for plasma simulation", *Computer Physics Communications*, vol. 222, pp. 351–373, 2017.

[38] A. Pukhov, "Particle-in-cell codes for plasma-based particle acceleration", Nov. 2016, pp. 181–206.

[39] G. Lapenta, "Kinetic plasma simulation: Particle in cell method", Aug. 2015.

[40] T. D. Arber, K. Bennett, C. S. Brady, *et al.*, "Contemporary particle-in-cell approach to laser-plasma modelling", *Plasma Physics and Controlled Fusion*, vol. 57, 2015.

[41] R. G. Hemker, "Particle-in-cell modeling of plasma-based accelerators in two and three dimensions", Ph.D. dissertation, University of California, Los Angeles, CA, 2000.

[42] C. K. Birdshall and A. B. Langdon, *Plasma Physics via Computer Simulation.* Great Yarmouth: IOP Publishing Ltd, 1991, ISBN: 0-07-005371-5.

[43] T. Z. Esirkepov, "Exact charge conservation scheme for particle-in-cell simulation with an arbitrary form-factor", *Computer Physics Communications*, vol. 135, no. 2, pp. 144–153, 2001.

[44] H. Ueda, Y. Omura, H. Matsumoto, and T. Okuzawa, "A study of the numerical heating in electrostatic particle simulations", *Computer Physics Communications*, vol. 79, pp. 249–259, 1994.

[45] R. Courant, K. Friedrichs, and H. Lewy, "On the partial difference equations of mathematical physics", *IBM Journal of Research and Development*, vol. 11, pp. 215–234, 1967.

[46] C. E. Shannon, "Communication in the presence of noise", *Proceedings of the IRE*, vol. 37, pp. 10–21, 1949.

[47] J. Psikal. "Particle-in-cell simulations of laser-plasma interactions". (2019), [Online]. Available: `http://kfe.fjfi.cvut.cz/~psikal/PowerLaPs/PICprednaska.pdf` (visited on 02/16/2023).

[48] Smilei. "Advanced numerical techniques". (2023), [Online]. Available: `https://smileipic.github.io/Smilei/Understand/numerical_techniques.html` (visited on 02/16/2023).

[49]   A. Lifschitz, X. Davoine, E. Lefebvre, J. Faure, C. Rechatin, and V. Malka, "Particle-in-cell modelling of laser–plasma interaction using fourier decomposition", *Journal of Computational Physics*, vol. 228, pp. 1803–1814, 2008.

[50]   J.-L. Vay, P. Colella, P. McCorquodale, B. V. Straalen, A. Friedman, and D. P. Grote, "Mesh refinement for particle-in-cell plasma simulations: Applications to and benefits for heavy ion fusion", *Laser and Particle Beams*, vol. 20, 2002.

[51]   J.-L. Vay, D. P. Grote, R. Cohen, and A. Friedman, "Novel methods in the particle-in-cell accelerator code-framework warp", *Computational Science and Discovery*, vol. 5, 2013.

[52]   J.-L. Vay, "An extended fdtd scheme for the wave equation: Application to multiscale electromagnetic simulation", *Journal of Computational Physics*, vol. 167, pp. 72–98, 2001.

[53]   J.-L. Vay, J.-C. Adam, and A. Heron, "Asymmetric pml for the absorption of waves. application to mesh refinement in electromagnetic particle-in-cell plasma simulations", *Computer Physics Communications*, vol. 164, pp. 171–177, 2004.

[54]   B. M. Cowan, D. L. Bruhwiler, E. Cormier-Michel, *et al.*, "Characteristics of an envelope model for laser–plasma accelerator simulation", *Journal of Computational Physics*, vol. 230, pp. 61–86, 2010.

[55]   S. Diederichs, C. Benedetti, A. Huebl, *et al.*, "Hipace++: A portable, 3d quasi-static particle-in-cell code", *Computer Physics Communications*, vol. 278, 2022.

[56]   C. M. Lazzarini, G. M. Grittani, P. Valenta, *et al.* "50 mev electron beams accelerated by a terawatt scalable khz laser". (2022), [Online]. Available: `https://arxiv.org/ftp/arxiv/papers/2302/2302.11415.pdf` (visited on 04/13/2023).

Appendices

A   Normalized units in Smilei

Reference quantity	Symbol	Units	Comment
velocity	V_r	c	the speed of light
charge	Q_r	e	the elemental charge
mass	M_r	m_e	the electron mass
momentum	P_r	$m_e c$	
energy, temperature	K_r	$m_e c^2$	
time	T_r	$\frac{1}{\omega_r}$	
length	L_r	$\frac{c}{\omega_r}$	
number density	N_r	$\varepsilon_0 m_e \frac{\omega_r^2}{e^2}$	the critical density
current density	J_r	ecN_r	
electric field	E_r	$m_e c \frac{\omega_r}{e}$	
magnetic field	B_r	$m_e \frac{\omega_r}{e}$	

Table 2: List of the most common normalizations used in Smilei.